Efficient sliding locomotion with isotropic friction

Silas Alben*
Department of Mathematics, University of Michigan, Ann Arbor, Michigan 48109, USA

(Received 11 February 2019; revised manuscript received 1 May 2019; published 4 June 2019)

Snakes' bodies are covered in scales that make it easier to slide in some directions than in others. This frictional anisotropy allows for sliding locomotion with an undulatory gait, one of the most common for snakes. Isotropic friction is a simpler situation (that arises with snake robots, for example) but is less understood. In this work we regularize a model for sliding locomotion to allow for static friction. We then propose a robust iterative numerical method to study the efficiency of a wide range of motions under isotropic Coulomb friction. We find that simple undulatory motions give little net locomotion in the isotropic regime. We compute general time-harmonic motions of three-link bodies and find three local optima for efficiency. The top two involve static friction to some extent. We then propose a class of smooth body motions that have similarities to concertina locomotion (including the involvement of static friction) and can achieve optimal efficiency for both isotropic and anisotropic friction.

DOI: 10.1103/PhysRevE.99.062402

I. INTRODUCTION

Snake locomotion has attracted the interest of biologists and engineers for several decades [1–6]. Many locomoting animals use appendages such as legs, wings, or fins to exert a force on the substrate or surrounding fluid to propel the rest of the body forward [7]. Snakes lack appendages, and thus it is less clear which parts of the snake body should exert propulsive forces and at which instants during the motion to move forward efficiently.

A typical way to understand how organisms move is to study physical or computational models and compare their motions with those of the actual organisms [7–11]. One can take a step further and pose and solve optimization problems for the models. This can suggest locomotion strategies that are effective for man-made vehicles [12–14]. It can also help understand why organisms have evolved in particular ways under a multitude of constraints [15–17].

Often what is optimized is a measure of the efficiency of locomotion. For example, one can maximize the average speed for a given time-averaged power expended by the organism. One can study the effects of physical parameters and constraints by varying them and studying how the optimal solutions change. Well-known examples are optimization studies of organisms moving in low- [18–24] and high-Reynolds-number fluid flows [25–31]. For locomotion in frictional (terrestrial or granular) media, frictional forces can result in distinctive modes of efficient (or optimal) locomotion [32–34].

Snakes are limbless reptiles with elongated bodies, supported by a backbone with 100–500 bony segments (vertebrae) [35]. The vertebrae allow for high flexibility, particularly in the lateral (side-to-side) direction, with less flexibility for vertical (dorso-ventral) bending or for torsion. Running along the backbone are muscles that attach to the sides of the vertebrae and cause bending. The snake body is covered in a skin with a compliance (stretchability) greater than that of mammalian skin and widely variable across species [36]. The outside of the skin is covered in hardened, keratinous scales. Scales on the belly are arranged so that friction is lower when the snake slides towards its head and higher when it slides towards its tail. Muscles attach to scales on the belly and can raise and lower them, modulating their frictional properties and providing a gripping ability [37].

On the basis of experiments and modeling, Hu *et al.* wrote that "Snake propulsion on flat ground, and possibly in general, relies critically on the frictional anisotropy of their scales" and measured the friction coefficients for snake specimens sliding in different directions: μ_f (for a snake sliding forward, towards the head), μ_b (sliding backward, towards the tail), and μ_t (sliding transverse to the body axis) [38]. It is difficult to measure friction coefficients for moving snakes, because their direction of motion and friction coefficients usually vary over their bodies. Hu *et al.* found $\mu_b \approx 1.3\mu_f$ and $\mu_t \approx 1.7\mu_f$ for corn and milk snakes on cloth [39]. Marvi and Hu measured forward and backward friction coefficients of corn snakes by placing them on styrofoam inclines and allowing them to slide head-first and tail-first under gravity [6]. They found $\mu_b \approx 1.6\mu_f$, and that conscious snakes' friction coefficients are about twice those of unconscious snakes, which were the focus of previous snake scale friction measurements [2,38]. When conscious, snakes can increase the angles of their scales to grip the surface, increasing friction. Hu and co-workers also studied the motions of snakes wearing cloth sleeves so that the scales do not contact the substrate, giving a representation of isotropic friction ($\mu_t = \mu_b = \mu_f$). They found that when the snakes undulate while wearing a sleeve, there is little if any forward motion [38,40].

Transeth *et al.* used experiments and simulations to show that for lateral undulation with isotropic friction, locomotion is possible but slow without barriers to push against [41,42].

*alben@umich.edu

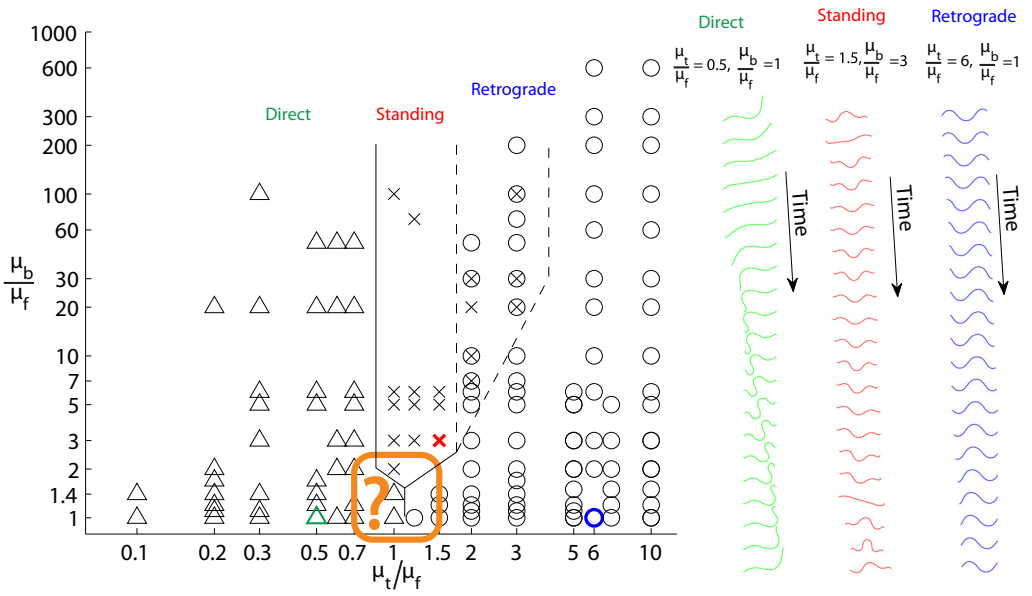

FIG. 1. Left: Classification of local optima across friction coefficient space, computed in [48]. Right: Three sequences of snapshots of locally optimal motions giving examples of direct, standing, and retrograde waves. These occur at particular friction coefficient ratios, listed above the snapshots and marked with green, red, and blue (light, medium, and dark gray) symbols in the panel at left. The three sequences of snapshots are given over one period of motion and are displaced vertically to enhance visibility but with the actual horizontal displacement.

Others have found that snake robots can achieve locomotion with isotropic friction using three-dimensional (3D) motions: sinus-lifting (slightly lifting the peaks of the body wave curve off the ground during lateral undulation), sidewinding, inchworm motions, and lateral rolling [43,44]. Chernousko simulated particular gaits of multilinked bodies with various friction coefficients and found that locomotion could be obtained with isotropic friction [45]. Wagner and Lauga studied the locomotion of a two-mass system moving in one dimension with isotropic friction (equal in the forward and backward directions) and found that locomotion is possible if the two masses have different friction coefficients and the length of the link connecting them has an asymmetric stroke cycle [46]. For the swimming of microorganisms in a viscous fluid (at zero Reynolds number), the drag anisotropy of long slender bodies and appendages is known to be essential for locomotion [47].

In a previous theoretical/computational study we optimized smooth snake-body kinematics for efficiency, starting from random initial ensembles [48]. The kinematics were described by the coefficients of a double series, Fourier in time (with unit period) and Chebyshev (polynomials) in arc length along the body axis, truncated at 45 modes (9 temporal by 5 spatial) and in some cases 190 modes (19 temporal by 10 spatial). The searches were begun at random points in the 45- and 190-dimensional spaces of these coefficients. We searched for smooth time-periodic body kinematics that maximize a definition of efficiency—the net distance traveled in one period divided by the work done against friction in one period [48]. The optimizers were calculated and classified as shown in Fig. 1, across the space of μ_t/μ_f (horizontal axis) and μ_b/μ_f (vertical axis). Many of the local optima could be classified as retrograde traveling waves—waves of curvature moving opposite to the body's direction of motion (i.e., lateral undulation)—prevalent for $\mu_t/\mu_f \gtrsim 6$; symmetric standing waves, observed for $\mu_b/\mu_f \geqslant 2$ and $0.7 < \mu_t/\mu_f \leqslant 3$; or direct waves—waves of curvature moving with the body's direction of motion—observed for $\mu_t/\mu_f \lesssim 0.7$. Direct waves have also been observed in the undulatory swimming of polychaete worms, with appendages extending perpendicular to the body axis [49,50]. Examples of these three classes of optima are shown in the snapshots on the right side of Fig. 1. In this study, one possible local optimum was observed with isotropic friction $\mu_b/\mu_f = \mu_t/\mu_f = 1$, but the efficiency gradient norm was reduced by only about 2 orders of magnitude from the random initial kinematics [48]. Usually computations did not converge to local optima in the vicinity of isotropic friction (orange box in Fig. 1). Because isotropic friction is common for snake robots (e.g., without scales) [44], is close to the measured friction coefficients for real snakes [39], and is physically the simplest situation, a better understanding of planar locomotion in this regime is useful. Isotropic friction is also a model of situations where snake scales are less effective—e.g., on loose, sandy, or slippery terrain [51]. Effective kinematics for planar locomotion with isotropic friction is the main topic of this study.

II. MODEL

We use the same Coulomb-friction snake model as Refs. [38,39,52] and other recent works. The snake body is thin compared to its length, so for simplicity we approximate its motion by that of a planar curve $\mathbf{X}(s,t) = (x(s,t), y(s,t))$, parametrized by arc length s and varying with time t. Schematic diagrams are shown in Fig. 2.

The tangent angle is denoted $\theta(s,t)$ and satisfies $\partial_s x = \cos\theta$ and $\partial_s y = \sin\theta$. The unit vectors tangent and normal to the curve are $\hat{\mathbf{s}} = (\partial_s x, \partial_s y)$ and $\hat{\mathbf{n}} = (-\partial_s y, \partial_s x)$, respectively. The basic problem is to prescribe the time-dependent shape of the snake in order to obtain efficient locomotion. We

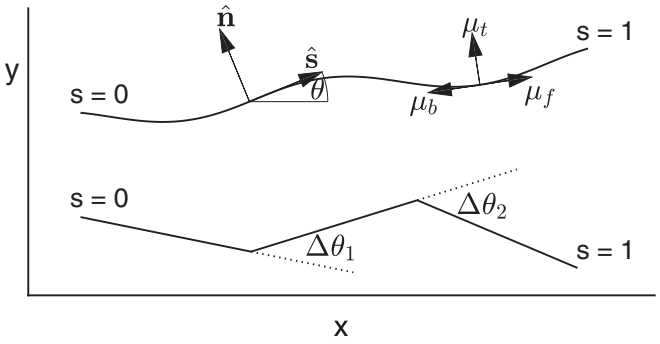

FIG. 2. Schematic diagrams of model snakes. Top: A smooth planar curve parametrized by arc length s (nondimensionalized by snake length) at an instant in time. The tangent angle and the unit vectors tangent and normal to the curve at a point are labeled. Vectors representing forward, backward, and transverse velocities are shown with the corresponding friction coefficients μ_f, μ_b, and μ_t. Bottom: A three-link snake with changes in angles $\Delta\theta_1$ (here positive) and $\Delta\theta_2$ (here negative) between the links.

consider both smooth bodies (Fig. 2, top) and three-link bodies (Fig. 2, bottom). The latter are described by $\Delta\theta_1$ and $\Delta\theta_2$, the differences between the tangent angles of the adjacent links.

We prescribe the body shape as $\Theta(s,t)$, the tangent angle in the "body frame," defined as a frame that rotates and translates so that at every time the body tail ($s=0$) lies at the origin in the body frame and the body has zero tangent angle at the tail ($\Theta(0,t)=0$). In the three-link case, $\Theta(s,t)=\Delta\theta_1(t)H(s-1/3)+\Delta\theta_2(t)H(s-2/3)$, where H is the Heaviside function. For all bodies (smooth and three link), the tangent angle in the physical (or laboratory) frame is obtained by adding $\theta_0(t)$, the actual tangent angle at the tail, to $\Theta(s,t)$:

$$\theta(s,t)=\theta_0(t)+\Theta(s,t). \tag{1}$$

The body position in the laboratory frame is then obtained by integration:

$$x(s,t)=x_0(t)+\int_0^s \cos\theta(s',t)ds', \tag{2}$$

$$y(s,t)=y_0(t)+\int_0^s \sin\theta(s',t)ds'. \tag{3}$$

The tail position $\mathbf{X}_0(t)=(x_0(t),y_0(t))$ and tangent angle $\theta_0(t)$ [or equivalently, $\dot{\mathbf{X}}_0(t)$ and $\dot{\theta}_0(t)$] are determined by the force and torque balance for the snake, i.e., Newton's second law:

$$\int_0^L \rho\partial_{tt}x ds=\int_0^L f_x ds, \tag{4}$$

$$\int_0^L \rho\partial_{tt}y ds=\int_0^L f_y ds, \tag{5}$$

$$\int_0^L \rho\mathbf{X}^\perp\cdot\partial_{tt}\mathbf{X} ds=\int_0^L \mathbf{X}^\perp\cdot\mathbf{f} ds. \tag{6}$$

Here L is the body length, ρ is the body's mass per unit length, and $\mathbf{X}^\perp=(-y,x)$. For simplicity, the body is assumed to be locally inextensible so L is constant in time. $\mathbf{f}$ is the force per unit length on the snake due to Coulomb friction with the ground:

$$\mathbf{f}(s,t)=-\rho g\mu_t(\widehat{\partial_t\mathbf{X}}\cdot\hat{\mathbf{n}})\hat{\mathbf{n}}-\rho g(\mu_f H(\widehat{\partial_t\mathbf{X}}\cdot\hat{\mathbf{s}}) + \mu_b[1-H(\widehat{\partial_t\mathbf{X}}\cdot\hat{\mathbf{s}})])(\widehat{\partial_t\mathbf{X}}\cdot\hat{\mathbf{s}})\hat{\mathbf{s}}. \tag{7}$$

Again, H is the Heaviside function and the hats denote normalized vectors. When $\|\partial_t\mathbf{X}\|=0$ we define $\widehat{\partial_t\mathbf{X}}$ to be $\mathbf{0}$. According to (7) the snake experiences friction with different coefficients for motions in different directions. The frictional coefficients are μ_f, μ_b, and μ_t for motions in the forward ($\hat{\mathbf{s}}$), backward ($-\hat{\mathbf{s}}$), and transverse (i.e., normal, $\pm\hat{\mathbf{n}}$) directions, respectively. In general, the snake velocity at a given point has both tangential and normal components, and the frictional force density has components acting in each direction. A similar decomposition of force into directional components occurs for viscous fluid forces on slender bodies [53]. In this paper we focus on efficient locomotion with isotropic friction and compare it to the anisotropic case. With isotropic friction, $\mu_f=\mu_b=\mu_t=\mu$, and (7) takes a much simpler form: $\mathbf{f}(s,t)=-\rho g\mu\widehat{\partial_t\mathbf{X}}$. The simpler formula does not simplify the computational methods (much) or the optimal motions, however. In this paper we compare motions under both isotropic and anisotropic friction, so we continue with the more general anisotropic form (7), which applies in both cases.

We assume that the body shape $\Theta(s,t)$ is periodic in time with period T, similar to the steady locomotion of real snakes [38]. We nondimensionalize Eqs. (4)–(6) by dividing lengths by the snake length L, time by T, and mass by ρL. Dividing both sides by g we obtain

$$\frac{L}{gT^2}\int_0^1 \partial_{tt}x ds=\int_0^1 f_x ds, \tag{8}$$

$$\frac{L}{gT^2}\int_0^1 \partial_{tt}y ds=\int_0^1 f_y ds, \tag{9}$$

$$\frac{L}{gT^2}\int_0^1 \mathbf{X}^\perp\cdot\partial_{tt}\mathbf{X} ds=\int_0^1 \mathbf{X}^\perp\cdot\mathbf{f} ds. \tag{10}$$

In (8)–(10) and from now on, all variables are dimensionless. If the body accelerations are not very large, as is often the case for robotic and real snakes [38], $L/gT^2\ll 1$, which means that the body's inertia is negligible. By setting inertia—and the left-hand sides of (8)–(10)—to zero, we simplify the equations considerably:

$$\int_0^1 f_x ds=\int_0^1 f_y ds=\int_0^1 \mathbf{X}^\perp\cdot\mathbf{f} ds=0. \tag{11}$$

In (11), the dimensionless force $\mathbf{f}$ is

$$\mathbf{f}(s,t)=-\mu_t(\widehat{\partial_t\mathbf{X}}\cdot\hat{\mathbf{n}})\hat{\mathbf{n}}-(\mu_f H(\widehat{\partial_t\mathbf{X}}\cdot\hat{\mathbf{s}}) + \mu_b[1-H(\widehat{\partial_t\mathbf{X}}\cdot\hat{\mathbf{s}})])(\widehat{\partial_t\mathbf{X}}\cdot\hat{\mathbf{s}})\hat{\mathbf{s}}. \tag{12}$$

Similar models were used in Refs. [32,38,39,48,52,54,55], and the same model was found to agree well with the motions of biological snakes in [38].

Figure 3 shows examples of the force-velocity relationship expressed by (12). Panel (a) shows the total frictional force $\mathbf{F}$ (red vector) on a flat plate with a 45-deg tangent angle and uniform horizontal velocity $\mathbf{v}$ (blue vector) for three different choices of friction coefficients. At the top is isotropic friction,

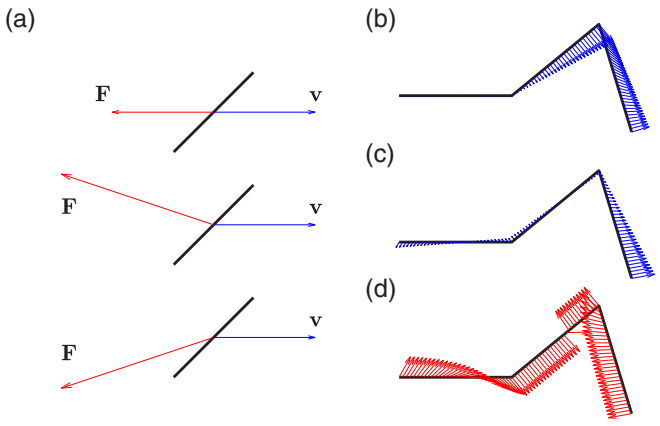

FIG. 3. (a) Frictional force **F** (red vector) acting on a flat plate moving uniformly with horizontal velocity **v** (blue vector) when the transverse friction coefficient μ_t is equal to (top), greater than (middle), or less than (bottom) the forward friction coefficient μ_f. (b) Velocity distribution (blue vectors) on a three-link body with zero translational and rotational velocities ($\dot{\mathbf{X}}_0$ and $\dot{\theta}_0$) at the tail (left endpoint). Here $\Delta\theta_1 = 39$ deg, $\Delta\theta_2 = -113$ deg, $\Delta\dot{\theta}_1 = -0.56$, and $\Delta\dot{\theta}_2 = 1$. (c) Velocity distribution in the laboratory frame: the translational and rotational velocities at the tail are such that the integrated force and torque due to the frictional force distribution [red vectors shown in panel (d)] are zero.

$\mu_f = \mu_t = 1$ (μ_b is not involved here since $\mathbf{v}\cdot\hat{\mathbf{s}} > 0$). With isotropic friction, **f** is directed opposite to **v**. The middle case has $\mu_f = 1$ and $\mu_t = 2$, increasing the force component in the $\hat{\mathbf{n}}$ direction. The bottom case has instead $\mu_f = 2$ and $\mu_t = 1$, increasing the force component in the $-\hat{\mathbf{s}}$ direction. Panel (b) shows an example of a motion of a three-link body where the tail velocities $\dot{x}_0(t)$, $\dot{y}_0(t)$, and $\dot{\theta}_0(t)$ are zero. Here $\Delta\theta_1$ is decreasing and $\Delta\theta_2$ is increasing in time, resulting in the nonuniform velocity distribution (piecewise linear in s) shown by the blue vectors. The force and torque balance equations are not satisfied by this motion. Panel (c) shows the same motion but with $\dot{x}_0(t)$, $\dot{y}_0(t)$, and $\dot{\theta}_0(t)$ chosen to satisfy Eq. (11). This adds a counterclockwise rotation and downward and leftward translation to the body. The resulting force distribution is shown by the red vectors in Fig. 3(d). The net force and torque from this distribution are zero. Although the velocities are small on the first two links, the forces are large—the normalization of velocities in (12) means that small velocities can give rise to $O(1)$ forces. The motion in panel (c) is approximately one in which only the third link is moving, rotating counterclockwise, but the small but nonzero velocities on the first two links are enough to give forces and torques that balance those on the third link.

Instead of solving (11) for $\{\mathbf{X}_0(t), \theta_0(t)\}$ directly, we solve them for $\{\dot{\mathbf{X}}_0(t), \dot{\theta}_0(t)\}$, which can be done (mostly) in parallel, speeding up the computations. Given $\Theta(s,t)$ and $\partial_t\Theta(s,t)$, we first solve (11) with $\theta_0(t) = 0$ and $\mathbf{X}_0(t) = 0$ to obtain a solution $\{\dot{\mathbf{X}}_{0b}(t), \dot{\theta}_{0b}(t)\}$ in the body frame for the unknowns $\{\dot{\mathbf{X}}_0(t), \dot{\theta}_0(t)\}$. We can solve for $\{\dot{\mathbf{X}}_{0b}(t), \dot{\theta}_{0b}(t)\}$ at all time steps in parallel, since only $\Theta(s,t)$ and $\partial_t\Theta(s,t)$ are required. Then we integrate $\dot{\theta}_0(t) = \dot{\theta}_{0b}(t)$ (equality shown in Appendix A) forward in time to obtain the tail tangent angle starting from $\theta_0(0) = 0$ (an arbitrary constant that sets the overall trajectory direction). Then we form $\mathbf{R}_{\theta_0(t)}$, the matrix that rotates by $\theta_0(t)$, and integrate $\dot{\mathbf{X}}_0(t) = \mathbf{R}_{\theta_0(t)}\dot{\mathbf{X}}_{0b}(t)$ (equality shown in Appendix A) forward in time starting from $\mathbf{X}_0(0) = 0$ (another arbitrary constant) to obtain the tail position in time. Then the complete body motion is known from (1)–(3). The equalities shown in Appendix A are due to the rotational invariance of the solutions to Eq. (11)—the body velocities are rotated when the coordinate system is rotated.

In this work we will consider only motions that involve zero net rotation over one period, i.e., $\theta_0(1) = \theta_0(0)$. Then the motion after one period is a pure translation, with all points on the body moving the same distance:

$$d = \sqrt{(x_0(1) - x_0(0))^2 + (y_0(1) - y_0(0))^2}. \tag{13}$$

The work done by the snake against friction over one period is

$$W = \int_0^1 \int_0^1 -\mathbf{f}(s,t)\cdot\partial_t\mathbf{X}(s,t)\,ds\,dt. \tag{14}$$

Consider a given motion $\Theta(s,t)$ with period 1. For an integer $n > 1$, the "sped-up" motion $\Theta(s,nt)$ has period $1/n$ and also period 1. The shape velocity $\partial_t\Theta(s,t)$ is multiplied by n under this time rescaling, and we show in Appendix B that the body velocity is also multiplied by n: $\partial_t\mathbf{X}(s,t) \to n\partial_t\mathbf{X}(s,nt)$ (the same would not be true with nonzero body inertia). Thus the net distance d and work W are also multiplied by n [since **f** in (14) involves normalized velocity, so it is unchanged]. Since d and W both scale with the speed of the motion, it makes sense to define an efficiency as

$$\lambda = \frac{d}{W}, \tag{15}$$

which is the same when a given motion is sped up or slowed down. A somewhat more general problem, not pursued here, is to find motions that maximize d for a given $W > 0$, and then vary W. For small W, only a limited set of periodic motions—those with small amplitude—can perform work W in a period. When W is large, large-amplitude motions can perform work W, but also small amplitude motions by repeating the motion a given number of times. Hence, as W becomes larger we consider a larger class of motions that can eventually approximate essentially any periodic motion.

To limit the number of parameters under consideration, our definition of work (and efficiency) does not include internal energy losses, e.g., due to viscoelasticity of muscles [32,34]. Such terms are sometimes subdominant to external work [31].

Next we will calculate W, d, and λ for certain examples of motions [i.e., $\Theta(s,t)$] with both isotropic ($\mu_f = \mu_t = \mu_b = 1$) and anisotropic friction. Then we will focus on the isotropic case. We will examine the class of time-harmonic three-link motions and then propose a class of smooth motions that optimize λ.

Equation (11) assumes only kinetic friction is involved, but in reality there is also static friction. In Fig. 4 we show an example of a motion for which the kinetic friction model has no solution. That is, for the $\Theta(s,t)$ corresponding to this motion (not given mathematically here), no choice of $\{\dot{x}_0(t), \dot{y}_0(t), \dot{\theta}_0(t)\}$ can solve Eq. (11). Initially the body is given by the solid line. The two flaps on the left side oscillate

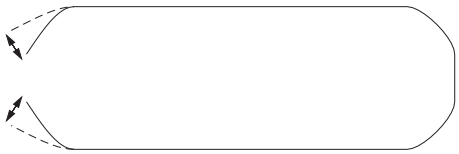

FIG. 4. Sketch of a body motion for which the kinetic friction model has no solution, so a model of static friction is used.

periodically, sweeping out a region shown by arrows between the solid line and the dashed lines. On the outward stroke, the combined vertical force and torque on the flaps from kinetic friction (12) is zero by symmetry, but there is a net horizontal force to the right. If we assume isotropic friction, the horizontal force per unit length on the flaps from (12) lies between 0 and 1, since the flaps move leftward and upward. The rest of the body cannot balance this force exactly for the following reasons. Its motion can only be horizontal to maintain vertical force balance. Therefore, by (12) it has horizontal force per unit length -1, 0, or $+1$, and a much larger length than the flaps. None of these choices gives zero net horizontal force on the body as a whole. The problem is resolved physically by including static friction: a force density between 0 and an order-1 constant when the velocity is zero [56]. Further examples will be given (for three-link bodies) in Sec. V (e.g., Fig. 10). In previous work with this model [38,39,48,52], only kinetic friction was used for simplicity. The kinetic friction model allows the snake motion to be computed for a wide range of $\Theta(s,t)$, such as traveling waves, without considering static friction. For such $\Theta(s,t)$, situations like that in Fig. 4 do not occur. When we optimized over a general class of smooth $\Theta(s,t)$ in [48] with the kinetic friction model only, algorithm breakdown due to unsolvability of the equations occurred occasionally, most often in the vicinity of isotropic friction.

Here we avoid the unsolvability of the equations and allow for static friction by using a simple modification of (12) involving a regularization parameter δ:

$$\mathbf{f}_\delta(s,t) \equiv -\mu_t(\widehat{\partial_t \mathbf{X}_\delta}\cdot\hat{\mathbf{n}})\hat{\mathbf{n}} - (\mu_f H(\widehat{\partial_t \mathbf{X}_\delta}\cdot\hat{\mathbf{s}}) + \mu_b[1-H(\widehat{\partial_t \mathbf{X}_\delta}\cdot\hat{\mathbf{s}})])(\widehat{\partial_t \mathbf{X}_\delta}\cdot\hat{\mathbf{s}})\hat{\mathbf{s}}, \tag{16}$$

$$\widehat{\partial_t \mathbf{X}_\delta} \equiv \frac{(\partial_t x, \partial_t y)}{\sqrt{\partial_t x^2 + \partial_t y^2 + \delta^2}}. \tag{17}$$

Here δ is small, 10^{-4} in our computations. We find empirically that there is little change in the results (less than 1% in relative magnitude) for δ in the range $(0, 10^{-4}]$. This is shown for three-link bodies in Appendix F by comparing values of velocity maps at different δ. When $\sqrt{\partial_t x^2 + \partial_t y^2}$ is similar in magnitude to δ, the force density in (16) varies between 0 and 1 in magnitude, times the appropriate friction coefficient. Therefore we obtain a range of force densities when velocities are very small which approximate static friction. In addition to their simplicity, we find empirically that expressions (16)–(17) have desirable properties, including the existence of unique solutions using the numerical algorithm described next. More specifically, for all motions shown in the work, our iterative numerical method (described next) finds a unique solution $\{\dot{x}_0(t), \dot{y}_0(t), \dot{\theta}_0(t)\}$ to Eq. (11) with $\mathbf{f}_\delta$ in place of $\mathbf{f}$ for a large number of initial guesses (covering a wide range including choices very far from the solution). Similar types of Coulomb friction regularization (sometimes involving the arctangent function) have been used for many years in dynamical simulations involving friction [57,58]. Many regularizations (including ours) involve a frictional force that rises monotonically from zero at zero velocity to the kinetic friction force [59–62]. Some regularizations (e.g., [63]) allow for a nonmonotonic behavior near zero velocity to simulate the effect of a static friction coefficient that is greater than the kinetic friction coefficient. These regularizations have been used to study stick-slip transitions for bodies with one degree of freedom (mass-spring systems). With a distributed frictional force density, our system is somewhat different, but we would expect the effect of such regularizations (such as stick-slip dynamics) to be limited to the vicinity of zero velocity. For our model, δ needs to be small compared to any physical velocities we wish to resolve. In particular, δ should be small compared to the speed of body deformations: the typical magnitude of $\partial_t\Theta(s,t)$ multiplied by the range of arc length in which it varies from zero.

III. NUMERICAL METHOD

In previous work [48], we computed solutions to Eq. (11) using quasi-Newton methods. Two major challenges of such methods are finding an initial guess that is sufficiently close to a solution for convergence and choosing a step size in the line search that moves an iterate towards a solution. The components of $\mathbf{f}_\delta$ behave like smoothed step functions near zero velocity. If the solution has velocities near zero (i.e., involves static friction), Newton's method requires a very good initial guess, within $O(\delta)$ of the solution, to converge. The behavior is similar to that for the arctangent function, a classic example used to illustrate the limited basin of attraction for Newton's method near a root [64,65].

To compute large numbers of solutions to (11) in parallel, we have developed a more robust iterative scheme that converges with any initial guess (for all cases studied, a large number including those in this work) and does not require a line search. The iteration is a fixed-point iteration using a linearization of the regularized version of Eq. (11). At time t, given $\Theta(s,t)$ and a guess $\{\dot{x}_0^n(t), \dot{y}_0^n(t), \dot{\theta}_0^n(t)\}$, we compute the corresponding $\{\partial_t x^n(s,t), \partial_t y^n(s,t), \partial_t \theta^n(s,t)\}$ [see Eqs. (A1) and (A2) in Appendix A] and then solve

$$\int_0^1 \tilde{f}_{\delta x} ds = \int_0^1 \tilde{f}_{\delta y} ds = \int_0^1 \mathbf{X}^\perp \cdot \tilde{\mathbf{f}}_\delta ds = 0 \tag{18}$$

for a new iterate $\{\dot{x}_0^{n+1}(t), \dot{y}_0^{n+1}(t), \dot{\theta}_0^{n+1}(t)\}$ where

$$\tilde{\mathbf{f}}_\delta(s,t) \equiv -\mu_t(\widetilde{\partial_t \mathbf{X}_\delta}\cdot\hat{\mathbf{n}})\hat{\mathbf{n}} - (\mu_f H(\widetilde{\partial_t \mathbf{X}_\delta}\cdot\hat{\mathbf{s}}) + \mu_b[1-H(\widetilde{\partial_t \mathbf{X}_\delta}\cdot\hat{\mathbf{s}})])(\widetilde{\partial_t \mathbf{X}_\delta}\cdot\hat{\mathbf{s}})\hat{\mathbf{s}}, \tag{19}$$

$$\widetilde{\partial_t \mathbf{X}_\delta} \equiv \frac{(\partial_t x^{n+1}, \partial_t y^{n+1})}{\sqrt{(\partial_t x^n)^2 + (\partial_t y^n)^2 + \delta^2}}. \tag{20}$$

Iterate n is used in the denominator of (20), so the new iterate $\{\dot{x}_0^{n+1}(t), \dot{y}_0^{n+1}(t), \dot{\theta}_0^{n+1}(t)\}$ appears only in the numerator, and

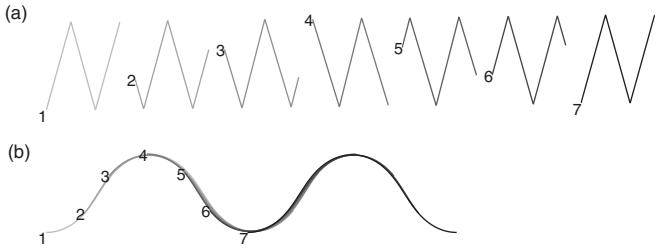

FIG. 5. Snapshots of the snake body when executing time-periodic traveling-wave body deformations (over one time period, darker at later times, labeled near the tail in numerical order). Top: Rightward-moving smoothed triangular deformation wave. Since $\mu_t = 1 \ll 100 = \mu_f$, the body moves rightward (i.e., a direct wave). The body tangent angle is $\approx \pm 1.3$ in the straight regions ($\Theta(s,t) = 1.3\tanh\{20\sin[2\pi(2s-t)]\}$). Bottom: Leftward-moving sinusoidal deformation wave with wavelength 1 ($\Theta(s,t) = \sin[2\pi(s+t)]$). Since $\mu_f = 1 \ll 100 = \mu_t$, the body moves rightward (i.e., a retrograde wave).

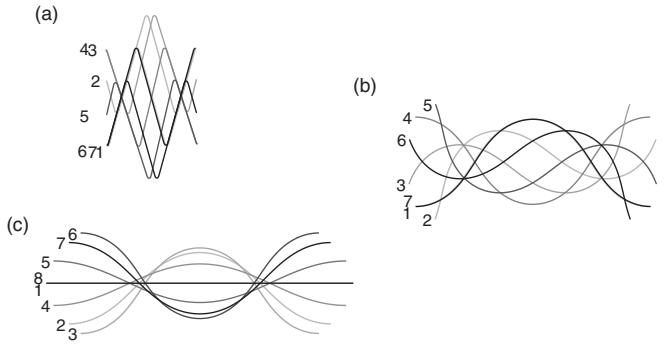

FIG. 6. Snapshots of the snake body over one time period (darker at later times, labeled near the tail in numerical order) when executing time-periodic body deformations with isotropic friction ($\mu_t = \mu_f = \mu_b = 1$). (a) Traveling wave with a smoothed triangular body shape (same as in Fig. 5(a) but with $\Theta(s,t) = 1.3\tanh\{20\sin[2\pi(1.5s-t)]\}$, slightly more smoothed for numerical accuracy). (b) Traveling wave with a sinusoidal tangent angle profile [same as in Fig. 5(b)]. (c) Standing wave with a sinusoidal tangent angle profile, $\Theta(s,t) = \sin(2\pi s)\sin(2\pi t)$.

Eqs. (18)–(20) depend linearly on it (in the body frame, where $\mathbf{X}$, $\hat{\mathbf{s}}$, and $\hat{\mathbf{n}}$ are known). Hence we obtain the new iterate $\{\dot{x}_0^{n+1}(t), \dot{y}_0^{n+1}(t), \dot{\theta}_0^{n+1}(t)\}$ by solving 3-by-3 linear systems at each t (decoupled when solving in the body frame). We observe empirically that this approach sacrifices the quadratic or superlinear convergence of Newton-type methods for linear (geometric) convergence. In almost all cases the convergence is quite fast, however. There are a small number of cases involving static friction where the rate of geometric convergence is slower. However, these cases are sufficiently few that even with more iterates, the cost of obtaining convergence is small. The loss of superlinear convergence is relatively modest compared to the increased simplicity and robustness of the algorithm. In Appendix D we explain how the algorithm is used to solve for body motions given $\Theta(s,t)$. In the next section we present body motions computed with this algorithm.

IV. EXAMPLES OF MOTIONS

We now present numerical solutions of the model described in Sec. II. We show motions that are approximately optimal with very anisotropic friction and then show how these motions perform with isotropic friction.

In Fig. 5(a) we show snapshots of the body when executing a rightward-moving smoothed triangular wave ($\Theta(s,t) = 1.3\tanh\{200\sin[2\pi(1.5s-t)]\}$) with friction much smaller in the transverse direction than in the tangential direction ($\mu_t = 1 \ll 100 = \mu_f = \mu_b$). The motion is almost entirely in the transverse direction, and due to the almost vertical body slope, the transverse direction is approximately horizontal, close to the direction of locomotion. The efficiency λ is 0.71 here. As the deformation wave is made steeper and μ_f is increased, the efficiency increases towards 1.

Figure 5(b) shows snapshots when the anisotropy is reversed ($\mu_f = 1 \ll 100 = \mu_t$), so friction is much smaller in the tangential direction (similar to snake robots that roll along the body axis [66]). Here $\mu_b = 1$ but is arbitrary since there is no backward motion. The body deforms as a sinusoidal leftward-moving wave ($\Theta(s,t) = \sin[2\pi(s+t)]$). The efficiency λ is 0.74, and can be made to approach 1 in the limit $\mu_t \to \infty$ by decreasing the amplitude and the deformation wavelength, so motion is almost purely in the tangential direction and in the direction of motion. Since $\mu_f = 1$, the work done per unit distance traveled tends to 1. Unlike in Fig. 5(a), here the wave shape (whether sinusoidal, triangular, etc.) does not matter in the limiting case of optimal efficiency. The motions in Figs. 5(a) and 5(b) are somewhat idealized versions of the direct and retrograde waves shown in Fig. 1 and are discussed in [48]. With large backward friction and $\mu_f \approx \mu_t \approx 1$, ratcheting motions were found to be locally optimal in that work. Now we show that with isotropic friction, none of these motions is effective.

In Figs. 6(a) and 6(b) we show snapshots from the same motions as in Figs. 5(a) and 5(b) but with isotropic friction ($\mu_f = \mu_t = \mu_b = 1$). Figure 5(c) shows a standing wave motion [$\Theta(s,t) = \sin(2\pi s)\sin(2\pi t)$], similar to those which were found to be effective with large backward friction in [48]. In all three cases the work done against friction is 0.4–0.6, but the distance traveled is less than 0.005, about the level of numerical error.

V. THREE-LINK TIME-HARMONIC MOTIONS

To increase our intuition about locomotion in the isotropic regime, we now study the efficiency of a broad range of motions. The space of time-periodic motions $\Theta(s,t)$ is infinite dimensional, so to make the problem tractable we look at a finite-dimensional subspace involving three-link bodies. These have been studied extensively in locomotion problems in the past (in a viscous fluid at zero Reynolds number) [18,20,67,68]. The optimally efficient motion found in [20] for zero-Reynolds-number swimming was close to a time-harmonic motion. Furthermore, Dai *et al.* found that optimal swimming in sand (which may behave like a fluid or solid in different settings) resembles optimal low-Reynolds-number swimming [69]. In previous work we studied the motions of two-link bodies with various friction coefficients and of three-link bodies with the anisotropic friction coefficients measured

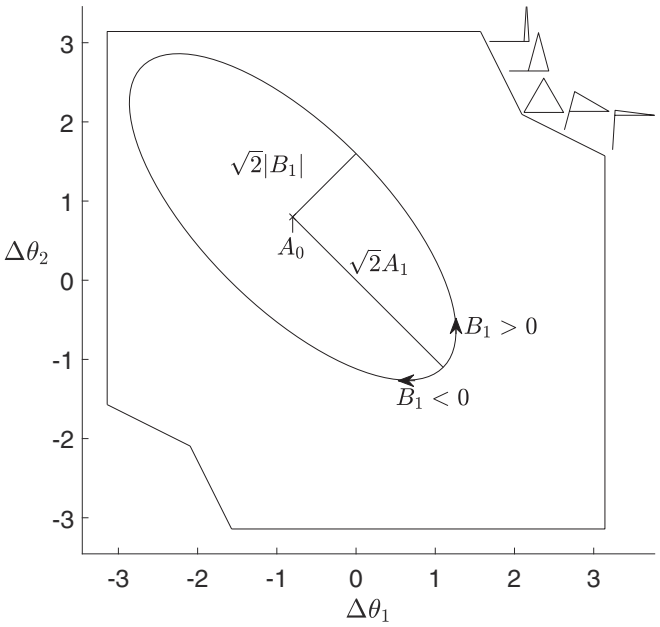

FIG. 7. A schematic diagram of an elliptical path in the space of non-self-intersecting configurations $(\Delta\theta_1, \Delta\theta_2)$ for a three-link body, symmetric about the line $\Delta\theta_1 = -\Delta\theta_2$. A_0 is the average of $\Delta\theta_1$ over the ellipse, and $\sqrt{2}A_1$ and $\sqrt{2}|B_1|$ are the semimajor and semiminor axes of the ellipse. The sign of B_1 gives the direction in which the path is traversed.

from real snakes [39] and found locally optimal motions [52]. Anisotropy played an important role in the above studies. Now, with an improved model involving static friction and an improved numerical method, we compute the full range of motions of three-link bodies with isotropic friction when the joint angles are time-harmonic functions.

The bodies' shape at an instant is described by only two joint angles $(\Delta\theta_1, \Delta\theta_2$; see Fig. 2), so the possible motions are a set of paths in a two-dimensional region shown in Fig. 7. The region is a square with sections removed at the upper-right and lower-left corners, where the body self-intersects (at the upper-right corner, five bodies are shown corresponding to configurations along the boundary of this section).

Within this space of paths, we consider a low-dimensional subspace—motions that have a single frequency (i.e., time-harmonic motions)—and are symmetric about the line $\Delta\theta_1 = -\Delta\theta_2$. This symmetry guarantees no net rotation over a period (see Appendix C), so the long time trajectory of the body is a straight line rather than a circle. Such paths are described by

$$\begin{aligned}\Delta\theta_1(t) &= A_0 + A_1\cos(2\pi t) + B_1\sin(2\pi t),\\ \Delta\theta_2(t) &= -A_0 - A_1\cos(2\pi t) + B_1\sin(2\pi t), \quad 0 \leqslant t \leqslant 1.\end{aligned} \tag{21}$$

The three parameters A_0, A_1, and B_1 describe an ellipse with center $(A_0, -A_0)$ and principal semiaxes A_0 and $|B_0|$ (Fig. 7). We assume $A_0 \geqslant 0$ without loss of generality, so the motion starts in the lower-right portion instead of the upper-left portion of the ellipse (but the same path is traversed in either case). The sign of B_1 gives the direction (clockwise or counterclockwise) around the path. Changing the sign of B_1 reverses time and thus reverses the motion (when $\mu_b = \mu_f$, as here), giving the same efficiency.

We compute motions over the region of (A_0, A_1, B_1) space giving admissible paths (ellipses that lie in the region of Fig. 7). To solve a large number of motions quickly, it is efficient to first compute a velocity map (or "connection" [52,70,71])—a map from the shape variables $(\Delta\theta_1, \Delta\theta_2)$ and their velocities $(\Delta\dot\theta_1, \Delta\dot\theta_2)$, to the body velocities at the tail $\{\dot x_0(t), \dot y_0(t), \dot\theta_0(t)\}$, from which we can reconstruct the body motion at each time [see Eqs. (A1) and (A2) in Appendix A] and thus the efficiency. The velocity maps are shown explicitly in Fig. 8. They are computed with the iterative method in Sec. III. Given these maps, the body motion for all possible (A_0, A_1, B_1)—and corresponding $(\Delta\theta_1, \Delta\theta_2, \Delta\dot\theta_1, \Delta\dot\theta_2)$—are then computed rapidly, in parallel, by interpolation of the data in Fig. 8, and integration in time. The more time-consuming iterative method is thus performed at a smaller set of points, a 65^3 grid ($\approx 3\times10^5$ data points) in the space of all possible $(\Delta\theta_1, \Delta\theta_2, \Delta\dot\theta_1, \Delta\dot\theta_2)$, and the less expensive interpolation and time integration are performed on the larger set of points spanning (A_0, A_1, B_1) and time—about 10^7 points for the data shown subsequently. In Appendix E we list the steps needed to solve for time-harmonic motions of three-link bodies using the velocity maps.

Multiplying $(\Delta\dot\theta_1, \Delta\dot\theta_2)$ by a constant simply multiplies $\{\dot x_0(t), \dot y_0(t), \dot\theta_0(t)\}$ by the same constant [see (B2) in Appendix (B)], so instead of computing $\{\dot x_0(t), \dot y_0(t), \dot\theta_0(t)\}$ over the four-dimensional space $(\Delta\theta_1, \Delta\theta_2, \Delta\dot\theta_1, \Delta\dot\theta_2)$, it is enough to compute the tail velocities over two three-dimensional spaces $(\Delta\theta_1, \Delta\theta_2, \Delta\dot\theta_1)$ with $|\Delta\dot\theta_1| \leqslant 1$ and $\Delta\dot\theta_2 = 1$, and $(\Delta\theta_1, \Delta\theta_2, \Delta\dot\theta_2)$ with $\Delta\dot\theta_1 = 1$ and $|\Delta\dot\theta_2| \leqslant 1$, and then obtain the tail velocities at other combinations of $(\Delta\dot\theta_1, \Delta\dot\theta_2)$ by rescaling them into one of these three-dimensional spaces. (If $\mu_b \neq \mu_f$ two additional maps would be needed, at $\Delta\dot\theta_1 = -1$ and $\Delta\dot\theta_2 = -1$).

In Fig. 8 we show the two sets of velocity maps used to construct $\{\dot x_0(t), \dot y_0(t), \dot\theta_0(t)\}$ for any values of body shape variables and their velocities when $\Delta\dot\theta_1 = 1$ (top row) and $\Delta\dot\theta_2 = 1$ (bottom row). For each map, the values of $\dot x_0(t)$, $\dot y_0(t)$, and $\dot\theta_0(t)$ are computed on a 65^3 grid in $\Delta\theta_1$–$\Delta\theta_2$–($\Delta\dot\theta_1$ or $\Delta\dot\theta_2$) space. With these maps we then compute the solutions $\{\dot x_0(t), \dot y_0(t), \dot\theta_0(t)\}$ for any choice of $(\Delta\theta_1, \Delta\theta_2, \Delta\dot\theta_1, \Delta\dot\theta_2)$ by interpolation. The data are shown as contours in six slice planes, which shows how solutions vary in the two horizontal dimensions $(\Delta\theta_1, \Delta\theta_2)$ and more roughly (with only six slice planes) in the vertical direction ($\Delta\dot\theta_1$ or $\Delta\dot\theta_2$). The first key point about the maps is that for three-link bodies, it is possible to visualize all the data needed to reconstruct their motion in a concise form, unlike for bodies with more degrees of freedom. One can identify features in the maps that could allow for further simplification of the models—the adjacent slice planes in Fig. 8 often have a similar contour patterns despite the large change (0.2) in the vertical axis parameter between slices—but we do not pursue this here for brevity. The second key point is that the contours are relatively smooth. Even though their shapes are not simple (due to the nonlinearity of the frictional forces), the maps show that interpolation is likely to be successful with a moderate number of data points (we find 65 in each dimension is sufficient) and this degree of smoothness in the data. We have observed from more extensive data that

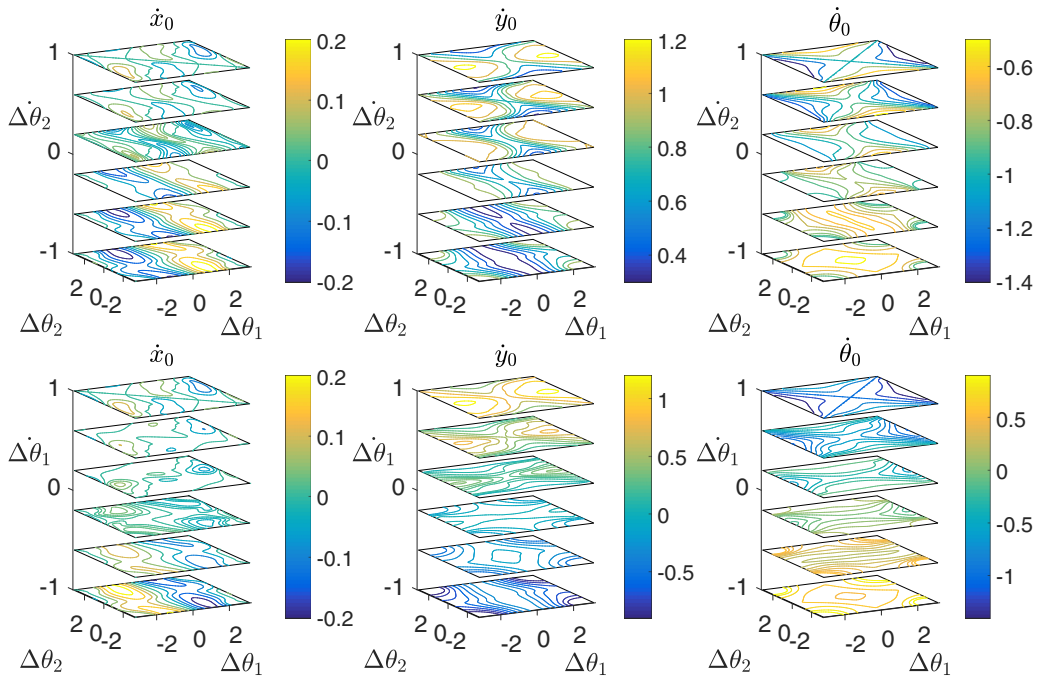

FIG. 8. Contour plots showing the three components of the velocity map ($\dot{x}_0$, $\dot{y}_0$, and $\dot{\theta}_0$) as functions of body shape and motion parameters (top row) $\Delta\theta_1$, $\Delta\theta_2$, and $\Delta\dot{\theta}_2$ when $\Delta\dot{\theta}_1 = 1$ or (bottom row) $\Delta\theta_1$, $\Delta\theta_2$, and $\Delta\dot{\theta}_1$ when $\Delta\dot{\theta}_2 = 1$.

$\{\dot{x}_0(t), \dot{y}_0(t), \dot{\theta}_0(t)\}$ are apparently continuous with bounded derivatives but that their derivatives change sharply where the regularization parameter is important, i.e., where static friction plays a role.

Static friction is potentially important when the speed ($\|\partial_t \mathbf{X}\|$) is of the order of the regularization parameter ($\delta = 10^{-4}$) over one or more entire links. If instead small velocities do not occur, or occur only at discrete points on the body, δ has only a small effect on the net forces and torque. In Fig. 9 we show regions in the velocity map spaces where static friction is important. Although the regions are small, they are involved in the motions that optimize efficiency, described in the next section. The regions can be classified into a small number of cases. Typical examples are shown in Figs. 9(c)–9(f), with corresponding labels in panel (a). Case (c) occurs when $\Delta\theta_1$ and $\Delta\theta_2$ are approximately equal to $\pi/2$ or $-\pi/2$. The forces from the outer links are nearly equal and opposite, but a small net force and torque is needed from the middle link to balance those on the outer links. Case (d) represents a broad region where one of the link angle velocities ($\Delta\dot{\theta}_1$ or $\Delta\dot{\theta}_2$) is zero and the other link angle is bent sharply (with magnitude between $\pi/2$ and π) and has nonzero velocity. Case (e) represents a smaller region where one of the link angles has a small but nonzero velocity. Case (f) occurs when the link angles have magnitudes near π and opposite signs. To understand why static friction is involved, we look at cases (c) and (f) more closely.

Figures 10(a) and 10(b) show symmetric examples similar to Figs. 9(c) and 4. The outer links provide forces that are nearly opposite and in the vertical direction but have a small horizontal component. Due to the top-bottom symmetry of the configuration, the velocity of the middle link can only be horizontal for the vertical forces to balance. Without regularization, the horizontal force per unit length on the middle link could only be 0 or ± 1, which cannot balance the small horizontal forces from the outer links. Regularization allows for a smaller horizontal force with a nearly static middle link, like the force from static friction. Figure 10(c) shows a symmetric version of Fig. 9(f)—symmetric with respect to reflection through the body center. The outer links provide forces that are equal and opposite but give a small net torque. To provide a torque with zero net force, the middle link has a purely rotational motion. Without regularization the force density on the middle link could only be 0, or–1 on one half and 1 on the other, giving a net torque of 0 or $\pm 1/36$ (since the link has length 1/3). Regularization allows a different torque to be obtained with a nearly static middle link, like that due to static friction. The other cases in Fig. 9 are more difficult to explain because they are not symmetric.

We now compute the distance traveled, work done, and their ratio λ, the efficiency, for the elliptical trajectories shown in Fig. 7, parametrized by A_0, A_1, and B_1. To aid our presentation we begin by showing in Fig. 11 the results in the two-parameter space with $A_0 = 0$. These are for motions that are symmetric with respect to the line $\Delta\theta_1 = \Delta\theta_2$, but there is no reason *a priori* to prefer such motions.

Figure 11(a) shows that the distance traveled per period is largest for a localized region of motion at the limit of self-contact. The dark blue region beyond the outer boundary of the shaded region gives coefficients for motions that involve self-contact. The distance is nearly zero for motions near the line $A_1 = B_1$, i.e., circular trajectories. These trajectories approximate the traveling-wave motions shown in the previous section and are effective for low-Reynolds-number swimming [18,20,67,68] given the 2:1 drag anisotropy of slender swimming bodies [47]. The line $A_1 = 0$ corresponds to standing-wave motions similar to that in the previous section and results in zero distance traveled, since the motion is the same but

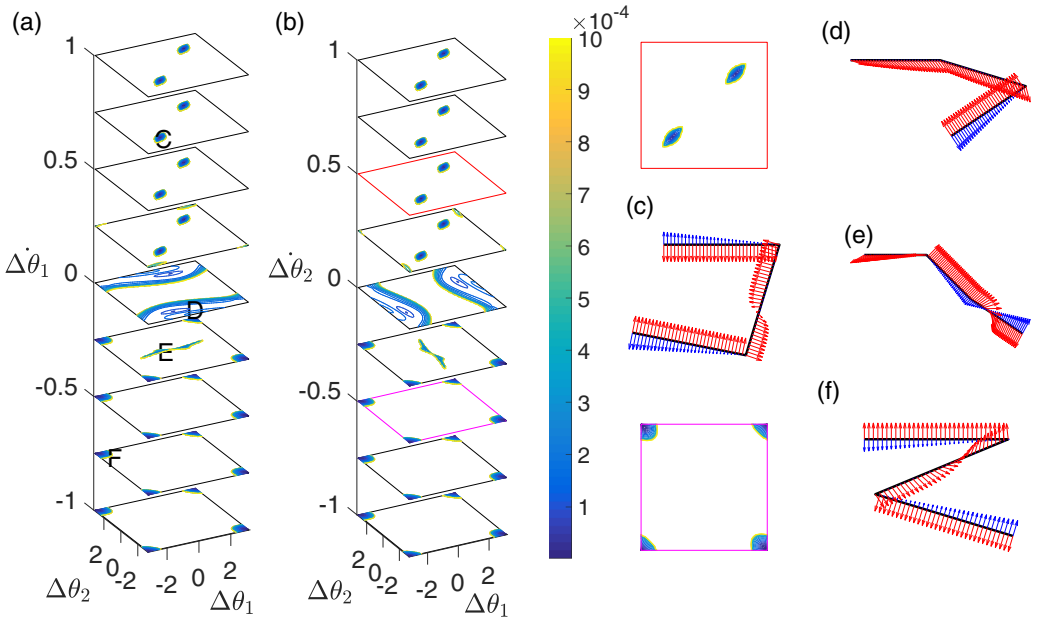

FIG. 9. Regions in the space of body shape and motion parameters where static friction regularization model is involved. (a, b) Contours show regions where the body speed lies between 0 and 10^{-3} over at least one of the three links, in the space of (a) $\Delta\theta_1$, $\Delta\theta_2$, and $\Delta\dot{\theta}_2$ when $\Delta\dot{\theta}_1 = 1$ or (b) $\Delta\theta_1$, $\Delta\theta_2$, and $\Delta\dot{\theta}_1$ when $\Delta\dot{\theta}_2 = 1$. The red and violet boxes show two examples of contour planes in 2D views at right. (c, d, e, f) Representative examples of body shapes and motions [labeled in (a)] where static friction regularization model is involved. Distributions of body velocities (blue, dark gray) and frictional forces (red, light gray) are shown.

the trajectory is reversed under time reversal. The line $B_1 = 0$ gives standing-wave motions that are antisymmetric about the body midpoint but also unchanged under time reversal, and thus they also give zero net distance traveled.

Figure 11(b) shows the work done per period, which has a much simpler distribution—it is nearly radially symmetric. Larger coefficients A_1 and B_1 are clearly correlated with larger sweeping motions of the links. The work done has no obvious relationship with the distance traveled (a), because the net translation (0.261 body lengths at maximum) is only a small contribution to the total motion in most cases. The efficiency (c) has a pattern similar to the distance, though, of course, smaller-amplitude motions are weighted more favorably. Nonetheless, the most efficient motion is close to the distance-maximizing motion and has efficiency 0.259. The quantities are invariant when the sign of B_1 is changed because the motion is simply reversed in time.

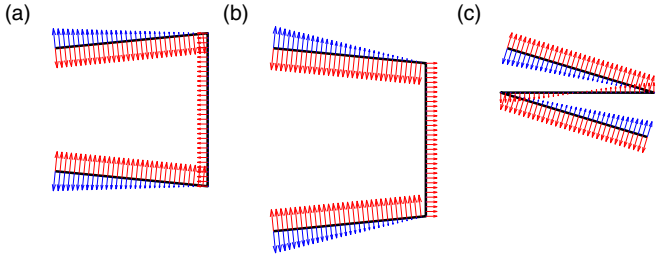

FIG. 10. Examples of symmetric body motions where the static friction regularization model is involved. Distributions of body velocities (blue) and frictional forces (red) are shown.

In Figs. 12(a)–12(c) we show the same quantities but with A_0 varied over its full range. At the middle of the A_0 axis is $A_0 = 0$, so there the contour plots (in red boxes) show the same data as in the previous figure. When $A_0 = 0$, the largest distance is achieved at a point with $A_1 > B_1$. As A_0 increases or decreases (moving up or down the vertical axis), another local maximum occurs, this one having $B_1 > A_1$. In panel (b), the work maintains an approximate radial symmetry, and does not depend strongly on A_0 (which varies the offset bias but not the sweeping amplitude of the links' motions). In panel (c), the efficiency has three local maxima. The global maximum is found at $A_0 = 0$, has efficiency 0.259, and is labeled "D" (here and in the previous figure). The motion is shown in panels (d) and (e). The second-best local optimum is found at $A_0 = 1.1$, has efficiency 0.207, and is labeled "F." The motion is shown in panels (f) and (g). The third local optimum (not shown) has $A_0 = 2.5$, efficiency 0.094. In panel (d), the snapshots of the globally optimal motion are arranged in two rows: first half-period (top) and second half-period (bottom), for which the body shape is a mirror image of that in first half-period (Θ has opposite sign). The snapshots are shown at equal time intervals during the half-periods (time is labeled at the bottom). At the top are four colored lines showing the speeds of the four endpoints of the three links versus time for the first half-period. We see that at two times, 0.07 and 0.43, three of the four endpoints (and two of the three links) are almost static. Here the static friction regularization is involved in the force balance. At $t = 0.07$, one link extends rightward while the other two remain fixed. At $t = 0.43$, one link is retracted rightward towards the other two. The snapshots are shown at their true locations in the laboratory frame in panel (e); the body moves about 0.26 body lengths.

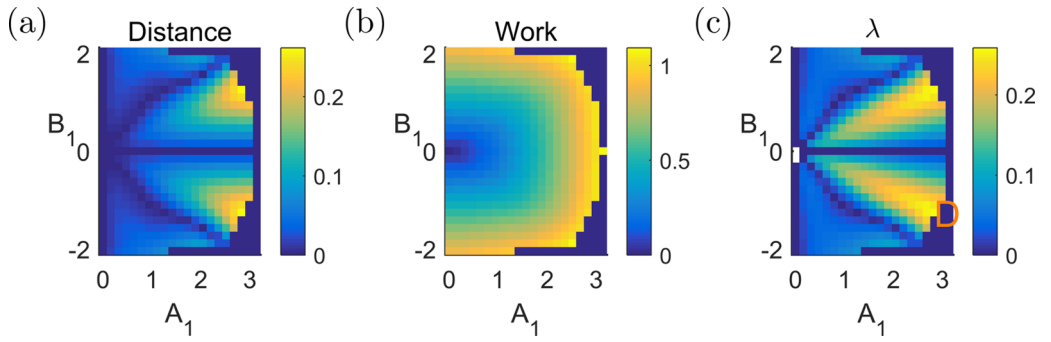

FIG. 11. Plots of (a) the distance traveled per period, (b) the work done against friction per period, and (c) the efficiency λ (distance/work) for elliptical paths with $A_0 = 0$.

For the second local optimum, the snapshots are shown in panel (f), in time increments of 0.05 over an entire period. Near $t = 0.33$ and 0.67, two of the links are almost static, while the third link moves in the direction of locomotion. The motion is shown in the laboratory frame in panel (g). The distance traveled is about 37% of that in panel (e) and the work done is about 47%. Both of the optimal motions can be described as follows: One of the outer links is rotated forward (i.e., in the direction of locomotion), with the other two mostly static [for $t = 0.38$–0.5 in (d), 0.2–0.5 in (f)],

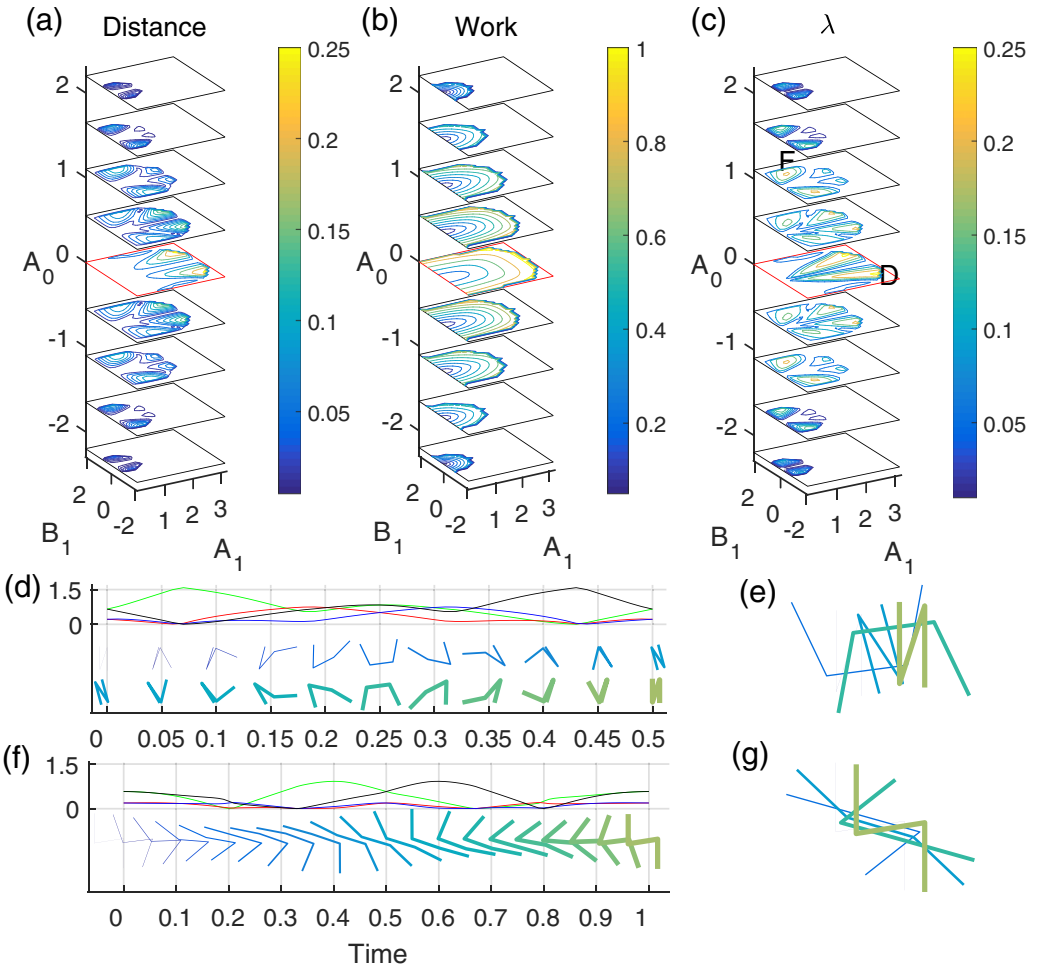

FIG. 12. Contour plots of (a) the distance traveled, (b) the work done against friction, and (c) the efficiency λ (distance/work) for elliptical paths with various A_0. (d) For the most efficient symmetric elliptical body motion [labeled "D" in panel (c) and Fig. 11(c)], the top four lines show the speeds of the four link endpoints (from tail to head: black, blue, red, and green). Below are snapshots of the body during the first (top row) and second (bottom row) half-periods. (e) A subset of snapshots from panel (d) in the laboratory frame. (f) For the motion giving the second best local optimum in efficiency [labeled "F" in panel (c)], the same data as in panel (d). (g) A subset of snapshots from panel (f) in the laboratory frame.

then the other outer link is rotated forward with the other two mostly static [from $t = 0-0.12$ in (d), 0.5–0.8 in (f)], then the middle link is moved, which requires the two outer links to rotate [from $t = 0.12-0.38$ in (d), 0.8–1 and 0–0.2 in (f)]. The motions are, roughly speaking, similar to concertina motion, where the snake moves part of its body (like one of the outer links) forward, pushing off of (or pulling towards) the rest of the body (like the other two links) that is held fixed by static friction, forming an "anchor" [1,3,72]. Because the body has only three links, moving the middle link forward requires all three links to move and rotate, so this part of the motion is somewhat distinct.

VI. OPTIMAL MOTIONS

We now look for more general smooth motions that can achieve the highest possible efficiency for any inextensible body, not necessarily one with three links. Because computational optimization is difficult in the isotropic regime [48], here we instead construct a theoretical solution that was inspired by the concertinalike motions in the previous section. Although the three-link optima are the inspiration for the theoretical solution, it is not easy to approximate the theoretical solution with a superposition of low-frequency and three-link modes (or low-degree polynomials as in [48]), so here we begin with a theoretical construction and then verify its optimality computationally.

First, we show that an upper bound on efficiency for any motion is the reciprocal of the smallest friction coefficient (1 in the isotropic case). The distance traveled by the body (13) is the same for all s, since the body moves as a translation without rotation after one period. Thus we can write

$$d = \left\| \int_0^1 \int_0^1 \partial_t \mathbf{X}(s,t) ds dt \right\|. \tag{22}$$

The work done against friction is (14) with $\mathbf{f}$ from (7). Let $u_s \equiv \partial_t \mathbf{X} \cdot \hat{\mathbf{s}}$ and $u_n \equiv \partial_t \mathbf{X} \cdot \hat{\mathbf{n}}$. We have

$$-\mathbf{f}(s,t) \cdot \partial_t \mathbf{X}(s,t) = \frac{\mu_t u_n^2 + \mu_s u_s^2}{\sqrt{u_s^2 + u_n^2}}, \tag{23}$$

where

$$\mu_s(s,t) \equiv \left(\mu_f H(\widehat{\partial_t \mathbf{X}} \cdot \hat{\mathbf{s}}) + \mu_b [1 - H(\widehat{\partial_t \mathbf{X}} \cdot \hat{\mathbf{s}})]\right). \tag{24}$$

Therefore

$$\begin{aligned} -\mathbf{f}(s,t) \cdot \partial_t \mathbf{X}(s,t) &\geqslant \min(\mu_t, \mu_f, \mu_b) \sqrt{u_s^2 + u_n^2} \\ &= \min(\mu_t, \mu_f, \mu_b) \|\partial_t \mathbf{X}(s,t)\| \end{aligned} \tag{25}$$

and

$$\begin{aligned} W &\geqslant \min(\mu_t, \mu_f, \mu_b) \int_0^1 \int_0^1 \|\partial_t \mathbf{X}(s,t)\| ds dt \\ &\geqslant d \ \min(\mu_t, \mu_f, \mu_b), \end{aligned} \tag{26}$$

so

$$\lambda = \frac{d}{W} \leqslant \frac{1}{\min(\mu_t, \mu_f, \mu_b)}. \tag{27}$$

This upper bound corresponds to a body that translates uniformly in the direction of lowest friction. Such a motion cannot have zero net force for nonzero friction, but we now show simple motions that satisfy the equations of motion and saturate this upper bound in the limit of a small parameter, for any choice of friction coefficients, including the isotropic case. These are concertinalike motions in the sense that part of the body forms an anchor, remaining static due to static friction, allowing the rest of the body to be pushed or pulled forward.

We first assume isotropic friction. The body is initially straight [see Fig. 13(a), top]. The motion has three stages. In stage one, a straight segment in the rear half of the body but near the midpoint [between the circle and triangle in Fig. 13(a)] forms a "bump." It deforms from straight to curved but keeping the tangent angles at its endpoints unchanged, so the endpoints get closer. This pulls the rear of the body forward, because the front portion (front half) of the body (the "anchor") is static due to static friction. If the front portion of the body slides with an $O(1)$ velocity, the rear portion of the body is not large enough to provide a balancing force. Therefore, the front portion of the body's velocity is $O(\delta)$. At the end of stage one [red body in panel (a)], the bump reaches its maximum amplitude. In stage two (from the red body to the blue body), the bump travels forward along the body to the region between the triangle and the square. The blue shape is thus a mirror image of the red shape. Here the body endpoints do not move, because the region away from the bump (left of the circle and right of the square) is an anchor. Stage three [from the blue body to the last straight configuration in (a)] is essentially the reverse of stage one—the bump flattens out, pushing the region in front of the square forward, with the back region of the body fixed because now it is an anchor. The net result is that the body has moved rightward some amount (which can be seen comparing the body endpoints over the sequence of motions). In addition to moving rightward, the body undergoes a much smaller vertical displacement and rotation because the bump is upward. To achieve a motion with zero net rotation (and zero net vertical displacement), we then perform the mirror image of the motion [panel (b)] for $0.5 \leqslant t \leqslant 1$, with $\Theta(s, t+0.5) = -\Theta(s,t)$. Then we see that the mirror image motion in the laboratory frame is a solution

$$\dot{\theta}_0(t+0.5) = -\dot{\theta}_0(t),\ \partial_t \theta(s, t+0.5) = -\partial_t \theta(s,t), \tag{28}$$

$$\dot{y}_0(t+0.5) = -\dot{y}_0(t),\ \partial_t y(s, t+0.5) = -\partial_t y(s,t), \tag{29}$$

$$\dot{x}_0(t+0.5) = \dot{x}_0(t),\ \partial_t x(s, t+0.5) = \partial_t x(s,t). \tag{30}$$

We have the same horizontal displacement but the vertical displacement and rotation are reversed. Figure 13(b) shows the snapshots in the simulation of the second half of the motion (at the beginning/end of the three stages only). The length of the bump (half the arc-length distance from the circle to the square) is a control parameter ϵ that we can shrink to zero. We show now that the distance traveled is proportional to ϵ, and the work done can be decomposed into two parts. The work done inside the bump region (left of the circle and right of the square) is proportional to ϵ^2 [blue squares in panel (c)]. The velocities in the bump region $\sim\epsilon$, the frictional force

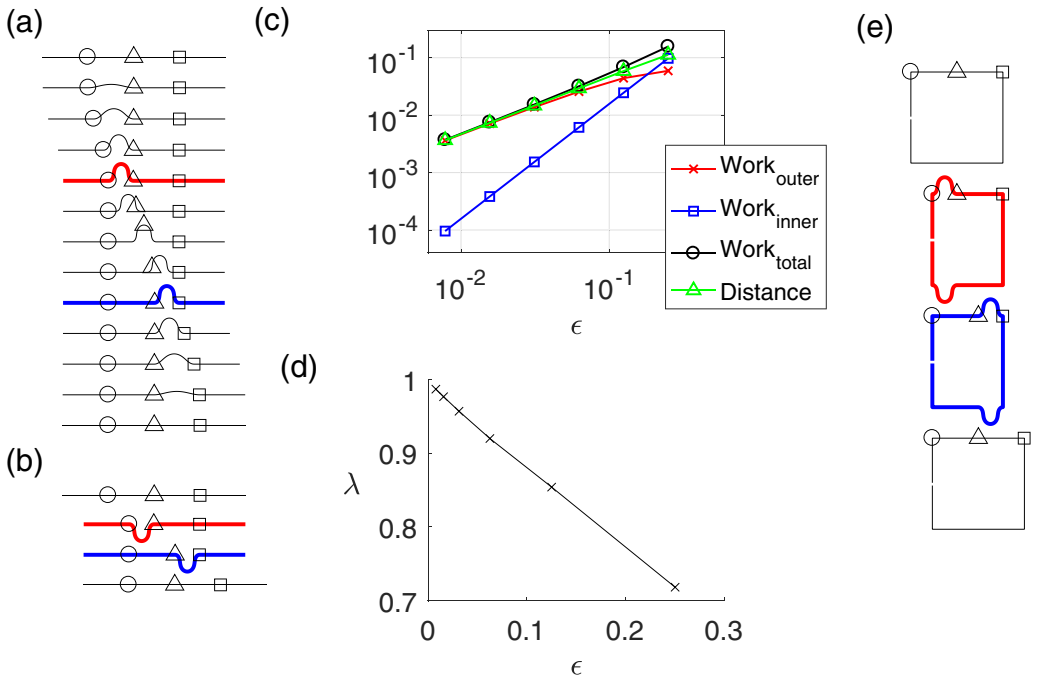

FIG. 13. Motions and performance of optimally efficient crawlers. (a) Snapshots of the crawler during the first half-period of motion. The circle and square are the endpoints of the bump region, and the triangle is the body midpoint. (b) Snapshots during the second half period. (c) Plot of work done against friction over one period outside the bump region ("$\text{Work}_{\text{outer}}$", red), that done inside the bump region ("$\text{Work}_{\text{inner}}$", blue), the total work (black), and the distance covered in one period (green) vs the bump region width parameter ϵ. (d) The efficiency $\lambda =$ Work/Distance vs the bump region length ϵ. (e) Snapshots of an efficient (symmetric) crawler when μ_t is the smallest friction coefficient.

density $\sim$1, and the bump region length $\sim\epsilon$, so by (14)

$$W_{\text{inner}} \sim \int_0^1 \int_{0.5-\epsilon}^{0.5+\epsilon} 1 \cdot \epsilon ds dt = O(\epsilon^2). \tag{31}$$

The work done outside the bump region [W_{outer}, red crosses in (c)] approaches the distance traveled (green triangles) as $\epsilon \to 0$, and both are proportional to ϵ. W_{outer} is approximately the unit frictional force density times the body speed in the region outside the bump multiplied by the length of that region $\sim$1:

$$W_{\text{outer}} \sim \int_0^1 \int_{\{0\leqslant s\leqslant 0.5-\epsilon\}\cup\{0.5+\epsilon\leqslant s\leqslant 1\}} 1 \cdot \partial_t x(s,t) ds dt \sim d. \tag{32}$$

Adding (31) and (32) we have $\lambda = 1 + O(\epsilon)$. This is shown in Fig. 13(d) for the motions in panels (a) and (b). When ϵ decreases below 0.1, we find it is necessary to decrease the numerical regularization parameter δ from 10^{-4} to 10^{-6} or 10^{-8} so it does not affect the results (i.e., so δ is much smaller than the typical speed of body deformation $\approx \epsilon$).

Now assume the friction coefficients are anisotropic. If the smallest friction coefficient is μ_f, then the head and tail should be at the right and left ends in panels (a) and (b). If instead μ_b is smallest, the head and tail should be reversed. If instead μ_t is the smallest friction coefficient, then we adopt the motion in panel (e). The body is bent into an approximate rectangle with two bump regions, and now the outer regions are oriented transverse to the direction of locomotion to take advantage of the lower friction with this orientation. By symmetry, net forces and torques are zero when the net motion is solely in the horizontal direction [the mirror image stroke in panel (b) is not required now]. The stages of motion are essentially the same as in panel (a), but for brevity, in panel (e) the snapshots are shown only at the beginning/end of each stage. With anisotropic friction, the above estimate for W_{inner} (31) is multiplied by $\max(\mu_t, \mu_f, \mu_b)$ to obtain an upper bound while that for W_{outer} (32) is multiplied by $\min(\mu_t, \mu_f, \mu_b)$. The global upper bound for λ (27) is achieved in the limit $\epsilon \to 0$.

We have assumed an inextensible body. For an extensible body, a one-dimensional version of the above motion is obtained by projecting the body density distribution at each instant onto the horizontal axis. Similar longitudinal motions are used by certain soft-bodied animals (e.g., worms) that alternately contract and extend longitudinal muscles [73]. Snakes, however, are nearly inextensible due to their backbone [35].

VII. CONCLUSION

In this work we have studied the locomotion of bending and sliding bodies under isotropic friction. In [48] we found that it is difficult to compute optimal motions in this regime with a model that uses kinetic friction. Therefore, in this paper we developed a regularization approach to handle cases where static friction is needed to find a solution. The previous optimization study [48] was also hampered by nonrobustness and occasional breakdown of the nonlinear solver for the body motion, particularly in the vicinity of isotropic friction. Therefore, in this paper we introduced a fixed-point iteration method that can compute the body tail velocities robustly from all initial guesses without the need for a line search

method. We first used the method to show that the most efficient motions with anisotropic friction—traveling-wave deformations—lead to little or no locomotion with isotropic friction. Next, we used the method to compute the velocity map for the three-dimensional body shape and shape velocity spaces of a three-link crawler. We used these maps to obtain a general picture of the locomotion efficiency landscape for the 3D space of coefficients giving symmetrical elliptical paths in the space of the body link angles. We found that static friction regularization is involved in small (but important) regions of the velocity map and described their necessity in symmetric cases. The distance traveled and efficiency are very small for motions corresponding to standing waves or traveling waves. The efficiency has three local maxima, and the top two (0.21 and 0.26) occur at motions that are similar to concertina locomotion—a sequence of motions in which one of the links moves forward while the other two links remain almost motionless.

We then proposed a class of concertinalike motions that saturate the upper bound for efficiency for any choice of friction coefficients. The optimal smooth motions of Sec. VI require short wavelengths $\sim\epsilon$ (and large frequencies $\sim 1/\epsilon$ to travel an $O(1)$ distance), which explains why the numerical optimization using 45 or 190 modes in [48] did not converge to such motions. It is interesting, however, that in the optimal time-harmonic motions with only three links, concertinalike motions can be seen. Although static friction arises in the optimal motions shown here, we believe that solutions with similar motions—and similar efficiencies—may exist with only the kinetic friction model (i.e., without regularization). In other words, the motion may be altered so that instead of remaining static, the "anchor" portion of the body slides slowly but has enough kinetic friction to balance that on the remainder of the body.

ACKNOWLEDGMENT

This research was supported by the NSF Mathematical Biology program under Award No. DMS-1811889.

APPENDIX A: INVARIANCE OF BODY VELOCITIES UNDER TRANSLATION AND ROTATION

We take the time derivatives of (1)–(3) using vector notation for position:

$$\partial_t \theta(s,t) = \dot\theta_0(t) + \partial_t \Theta(s,t), \tag{A1}$$

$$\partial_t \mathbf{X}(s,t) = \dot{\mathbf{X}}_0(t) + \int_0^s (\dot\theta_0(t) + \partial_t\Theta(s,t))\hat{\mathbf{n}}\,ds'. \tag{A2}$$

Given $\Theta(s,t)$ and $\partial_t\Theta(s,t)$, we first solve (11) with $\theta_0(t) = 0$ and $\mathbf{X}_0(t) = 0$ to obtain a solution $\{\dot{\mathbf{X}}_{0b}(t), \dot\theta_{0b}(t)\}$ in the body frame for the unknowns $\{\dot{\mathbf{X}}_0(t), \dot\theta_0(t)\}$ in (A1) and (A2). The solution $\{\dot{\mathbf{X}}_{0b}(t), \dot\theta_{0b}(t)\}$ represents the tail velocity if the body is rotated by $-\theta_0(t)$ so that the tail has zero tangent angle. The position $\mathbf{X}$ and tangent and normal vectors $\hat{\mathbf{s}}, \hat{\mathbf{n}}$ in the laboratory frame are simply those in the body frame rotated by $\theta_0(t)$. If we set $\dot\theta_0(t) = \dot\theta_{0b}(t)$ and let $\dot{\mathbf{X}}_0(t)$ be $\dot{\mathbf{X}}_{0b}(t)$ rotated by $\theta_0(t)$, then we find that the laboratory frame velocity $\partial_t\mathbf{X}$ in (A2) is the body frame velocity rotated by $\theta_0(t)$. Hence $\mathbf{f}$ in (12) is that in the body frame rotated by $\theta_0(t)$ and $\mathbf{X}^\perp\cdot\mathbf{f}$ is unchanged (this dot product and those in $\mathbf{f}$ are unchanged by the rotation)—so both $\mathbf{f}$ and $\mathbf{X}^\perp\cdot\mathbf{f}$ still integrate to zero under the transformation from the body to laboratory frame. To summarize, if $\{\dot{\mathbf{X}}_{0b}(t), \dot\theta_{0b}(t)\}$ solve (11) with $\{\mathbf{X}_0(t), \theta_0(t)\}$ equal to zero (i.e., in the body frame), then $\dot{\mathbf{X}}_0(t) = \mathbf{R}_{\theta_0(t)}\dot{\mathbf{X}}_{0b}(t)$ and $\dot\theta_0(t) = \dot\theta_{0b}(t)$ solve (11) with general $\{\mathbf{X}_0(t), \theta_0(t)\}$ when the body is also rotated by $\theta_0(t)$ (i.e., the body is in the laboratory frame). Here

$$\mathbf{R}_{\theta_0(t)} = \begin{pmatrix} \cos\theta_0(t) & -\sin\theta_0(t) \\ \sin\theta_0(t) & \cos\theta_0(t) \end{pmatrix}, \tag{A3}$$

the matrix that rotates by $\theta_0(t)$.

APPENDIX B: RESCALING OF MOTIONS UNDER RESCALING OF TIME

When the body shape motion $\Theta(s,t)$ is uniformly sped up or slowed down, i.e., when

$$\Theta(s,t) \to \Theta(s,ct), \quad \partial_t\Theta(s,t) \to c\,\partial_t\Theta(s,ct) \tag{B1}$$

for some constant $c > 0$, then the force and torque balance equations are satisfied when the tail motion undergoes the same scaling:

$$\{x_0(t), y_0(t), \theta_0(t)\} \to \{x_0(ct), y_0(ct), \theta_0(ct)\},$$
$$\{\dot x_0(t), \dot y_0(t), \dot\theta_0(t)\} \to c\{\dot x_0(ct), \dot y_0(ct), \dot\theta_0(ct)\}, \tag{B2}$$

and so does the overall body motion:

$$\mathbf{X}(s,t) \to \mathbf{X}(s,ct), \quad \partial_t\mathbf{X}(s,t) \to c\,\partial_t\mathbf{X}(s,ct). \tag{B3}$$

We can see this by first plugging the transformed quantities into (A1) and (A2) to verify that those equations are still obeyed. We also have $\widehat{\partial_t\mathbf{X}}(s,t) \to \widehat{\partial_t\mathbf{X}}(s,ct)$, and so the frictional force $\mathbf{f}(s,t) \to \mathbf{f}(s,ct)$ by (12), assuming $c > 0$ (note that $\hat{\mathbf{s}}(s,t) \to \hat{\mathbf{s}}(s,ct)$ and $\hat{\mathbf{n}}(s,t) \to \hat{\mathbf{n}}(s,ct)$), and the torque density $\mathbf{X}^\perp\cdot\mathbf{f}$ has the same transformation. If $\mu_b = \mu_f$ then the $H(\widehat{\partial_t\mathbf{X}}\cdot\hat{\mathbf{s}})$ term drops out of $\mathbf{f}$ in (12) and the same scaling holds for $c < 0$ also ($\mathbf{f}$ changes sign uniformly in this case). If instead $\mu_b \neq \mu_f$, then the solutions are not simply time reversed when the shape change is time reversed.

APPENDIX C: ZERO NET ROTATION FOR MOTIONS SYMMETRIC WITH RESPECT TO $\Delta\theta_1 = -\Delta\theta_2$

We show here that motions of three-link bodies that are symmetric with respect to the line $\Delta\theta_1 = -\Delta\theta_2$ (e.g., Fig. 7) result in zero net rotation over a period. For such motions we can assume (as in Sec. V) that the body motion starts on the line $\Delta\theta_1 = -\Delta\theta_2$ in configuration space (by shifting time by a constant if necessary), so the body lies on this line at $t = 0$ and 1, and at $t = 1/2$ by the symmetry of the path. The symmetry implies that the link angle differences at t and $1-t$ are related by $\Delta\theta_1(t) = -\Delta\theta_2(1-t)$ and $\Delta\theta_2(t) = -\Delta\theta_1(1-t)$. Thus if the three links at time t have tangent angles $\{\theta_0(t), \theta_0(t) + \Delta\theta_1(t), \theta_0(t) + \Delta\theta_1(t) + \Delta\theta_2(t)\}$, then those at $1-t$ have tangent angles $\{\theta_0(1-t), \theta_0(1-t) - \Delta\theta_2(t), \theta_0(1-t) - \Delta\theta_2(t) - \Delta\theta_1(t)\}$. This implies that $\theta(s,t) - \theta(1-s, 1-t) = \theta_0(t) + \Delta\theta_1(t) + \Delta\theta_2(t) - \theta_0(1-t)$, which is independent of s. In other words, the body at time $1-t$ has the same

shape (tangent angle) as that at time t, up to an overall rotation, when the body at time $1-t$ is viewed from the opposite end—starting at $s=1$ and ending at $s=0$. If we define a new coordinate $u=1-s$, we can describe the tangent angle at time $1-t$ in a body frame running from $u=0$ to $u=1$ using the function $\Theta_u(u,t)$ as

$$\theta(u,1-t)=\theta_{u=0}(1-t)+\Theta_u(u,1-t). \tag{C1}$$

We have $\Theta(s,t)=\Theta_u(1-s,1-t)$ and $\partial_t\Theta(s,t)=-\partial_t\Theta_u(1-s,1-t)$, so in the body frames the two shapes are the same and their rates of change are opposite. Therefore, following the solution procedure described below Eqs. (A1) and (A2), the solutions for the rotation rates at $s=0$ and $u=0$ are opposite (if $\mu_b=\mu_f$):

$$\dot\theta_{s=0,b}(t)=-\dot\theta_{u=0,b}(1-t). \tag{C2}$$

Here b denotes body frame, but these are also the rotation rates in the laboratory frame as discussed below Eqs. (A1) and (A2):

$$\dot\theta_{s=0}(t)=\dot\theta_{s=0,b}(t)=-\dot\theta_{u=0,b}(1-t)=-\dot\theta_{u=0}(1-t). \tag{C3}$$

We can use these results to compute the net rotation from $t=0$ to $t=1$ (over a period), $\theta_{s=0}(1)-\theta_{s=0}(0)$. Since the body has $\Delta\theta_1=-\Delta\theta_2$ at $t=0$, $1/2$, and 1, at those times the tangent angle at $u=0$ (in the direction of increasing u) is that at $s=0$ plus π:

$$\begin{aligned}
&\theta_{s=0}(1)-\theta_{s=0}(0)\\
&\quad=\theta_{u=0}(1)+\pi-\theta_{u=0}(1/2)\\
&\qquad+\theta_{u=0}(1/2)-\theta_{s=0}(0) &\text{(C4)}\\
&\quad=\theta_{u=0}(1)-\theta_{u=0}(1/2)+\theta_{s=0}(1/2)-\theta_{s=0}(0) &\text{(C5)}\\
&\quad=\int_{1/2}^{1}\dot\theta_{u=0}(t)dt+\int_{0}^{1/2}\dot\theta_{s=0}(t)dt &\text{(C6)}\\
&\quad=\int_{1/2}^{1}-\dot\theta_{s=0}(1-t)dt+\int_{0}^{1/2}\dot\theta_{s=0}(t)dt &\text{(C7)}\\
&\quad=\int_{1/2}^{0}\dot\theta_{s=0}(w)dw+\int_{0}^{1/2}\dot\theta_{s=0}(t)dt &\text{(C8)}\\
&\quad=0, &\text{(C9)}
\end{aligned}$$

where $w=1-t$. In words, whatever rotation occurs from $t=0$ to $1/2$ is undone from $1/2$ to 1, when we view the body from the opposite end.

APPENDIX D: ALGORITHM TO SOLVE FOR BODY MOTIONS GIVEN $\Theta(s,t)$ (e.g., SMOOTH BODY MOTIONS IN FIGS. 5, 6, AND 13)

Inputs:
(1) Body shape functions $[\Theta(s,t),\ \dot\Theta(s,t)]$ for all $t\in[0,\Delta t,\ldots,1]$,
(2)Body position in body frame $[\mathbf{X}_b(s,t)=\int_0^s(\cos\Theta(s',t),\sin\Theta(s',t))ds']$
(3) Initial guess (arbitrary, e.g., zero) for tail velocities $\{\dot x_0^0(t),\dot y_0^0(t),\dot\theta_0^0(t)\}$
(4) Tolerance $\eta\ll 1$.

Output: Body position in laboratory frame ($\mathbf{X}(s,t)$).
(1) For $n=0,1,2,\ldots$
At all $t\in[0,\Delta t,\ldots,1]$ (in parallel),
(a) Compute $\partial_t\mathbf{X}^n(s,t)$ using (A2) with $\{\dot x_0^n(t),\dot y_0^n(t),\dot\theta_0^n(t)\}$ and $\hat{\mathbf{n}}$ in the body frame.
(b) Solve the three equations (18) for the three unknowns $\{\dot x_0^{n+1}(t),\dot y_0^{n+1}(t),\dot\theta_0^{n+1}(t)\}$ by Gaussian elimination (the equations are linear in the three unknowns).
(c) Stop when the norms of the integrals in (18) with $\partial_t\mathbf{X}^n$ changed to $\partial_t\mathbf{X}^{n+1}$ (i.e., the nonlinear residuals at iterate $n+1$) are less than η.
End
(2) The computed rotational tail velocity in the body frame is $\dot\theta_{0b}(t)=\dot\theta_0^{n+1}(t)$, the same as the rotational tail velocity in the laboratory frame $\dot\theta_0(t)$. Integrate it to obtain $\theta_0(t)$.
(3) The computed $\dot{\mathbf{X}}_{0b}(t)$ is $\dot{\mathbf{X}}_0^{n+1}(t)$. Integrate $\dot{\mathbf{X}}_0(t)=\mathbf{R}_{\theta_0(t)}\dot{\mathbf{X}}_{0b}(t)$ to obtain $\mathbf{X}_0(t)$.
(4) Integrate (A2) to obtain $\mathbf{X}(s,t)$.

APPENDIX E: ALGORITHM TO SOLVE FOR TIME-HARMONIC MOTIONS OF THREE-LINK BODIES USING INTERPOLATION (E.G., FIGS. 8–12)

Inputs:
(1) A discrete array of values of $(\Delta\theta_1,\Delta\theta_2)\in$ feasible region (Fig. 7), and a discrete array of values of $\dot\Delta\theta_1$ (or $\dot\Delta\theta_2$) $\in[-1,1]$ and $\dot\Delta\theta_2$ (or $\dot\Delta\theta_1$ respectively) $=1$.
(2) A discrete array of values of the coefficients (A_0,A_1,B_1) in (21).
Outputs:
(1) Computed velocity maps

$$(\Delta\theta_1,\Delta\theta_2,\dot\Delta\theta_1)\to\{\dot x_0(t),\dot y_0(t),\dot\theta_0(t)\}\text{ with }\ \dot\Delta\theta_2=1 \tag{E1}$$

$$(\Delta\theta_1,\Delta\theta_2,\dot\Delta\theta_2)\to\{\dot x_0(t),\dot y_0(t),\dot\theta_0(t)\}\text{ with }\ \dot\Delta\theta_1=1 \tag{E2}$$

(2) Body position in laboratory frame $[\mathbf{X}(s,t)]$
(a) All points on the $(\Delta\theta_1,\Delta\theta_2,\dot\Delta\theta_{1/2})$ grid in parallel form $\Theta(s)=\Delta\theta_1H(s-1/3)+\Delta\theta_2H(s-2/3)$ and $\dot\Theta(s)=\dot\Delta\theta_1H(s-1/3)+\dot\Delta\theta_2H(s-2/3)$. Use these in place of $\Theta(s,t)$, $\dot\Theta(s,t)$ in step 1 (the iterative algorithm) in Appendix D to compute $\{\dot x_0(t),\dot y_0(t),\dot\theta_0(t)\}$. These are the values of the velocity maps.
(b) Given a set of link angle motions, e.g. of the form (21) for a set of (A_0,A_1,B_1) values, use interpolation within the velocity maps to find $\{\dot x_0(t),\dot y_0(t),\dot\theta_0(t)\}$ that correspond to each choice of (A_0,A_1,B_1) and t.
(c) Perform the integrations in steps 2–4 in Appendix D with $\{\dot x_0(t),\dot y_0(t),\dot\theta_0(t)\}$ to obtain $\mathbf{X}(s,t)$ for each choice of (A_0,A_1,B_1).
Comment: Using this algorithm on a single processor, with $\Delta t=0.01$ and a grid with spacing $\pi/20$ in (A_0,A_1,B_1), the computations needed to produce the data in Fig. 12 require tens of seconds using the velocity map and interpolation. Without the velocity map and only the algorithm in Appendix D, the time is several minutes.

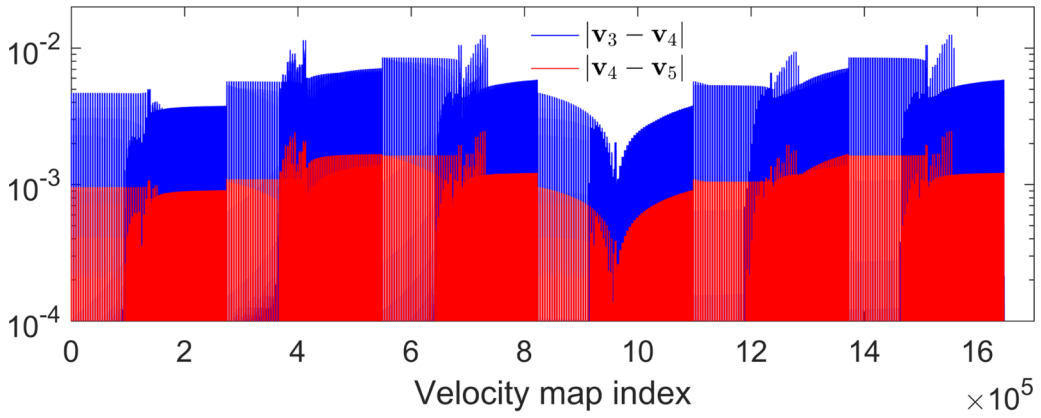

FIG. 14. Comparison of values of $\{\dot{x}_0(t), \dot{y}_0(t), \dot{\theta}_0(t)\}$ in velocity maps (E1) and (E2) for $\delta = 0.001$ ($\mathbf{v}_3$), $\delta = 0.0001$ ($\mathbf{v}_4$), and $\delta = 10^{-5}$ ($\mathbf{v}_5$).

APPENDIX F: EFFECT OF δ REGULARIZATION

Figure 14 compares the values of the velocity maps for $\delta = 0.001$ ($\mathbf{v}_3$), $\delta = 0.0001$ ($\mathbf{v}_4$), and $\delta = 10^{-5}$ ($\mathbf{v}_5$). Each $\mathbf{v}_i$ is a vector containing the values of $\{\dot{x}_0, \dot{y}_0, \dot{\theta}_0\}$ for each choice of (A_0, A_1, B_1) in a 65^3 grid, for the velocity maps (E1) and (E2), concatenated. Because there are three values $\{\dot{x}_0, \dot{y}_0, \dot{\theta}_0\}$ at each of the 65^3 points and two velocity maps, each $\mathbf{v}_i$ has length 6×65^3.

The difference $|\mathbf{v}_4 - \mathbf{v}_5|$ is about $\sqrt{10}$ less than $|\mathbf{v}_3 - \mathbf{v}_4|$ at each index, indicating that results converge as $\sqrt{\delta}$. The maximum value of $|\mathbf{v}_4 - \mathbf{v}_5|$ is about 0.0025, indicating the magnitude of error in $\mathbf{v}_4$, the velocity map values used in this paper.

[1] J. Gray, The mechanism of locomotion in snakes, J. Exp. Biol. **23**, 101 (1946).

[2] J. Gray and H. W. Lissmann, The kinetics of locomotion of the grass-snake, J. Exp. Biol. **26**, 354 (1950).

[3] B. C. Jayne, Kinematics of terrestrial snake locomotion, Copeia 915 (1986).

[4] J. J. Socha, Kinematics: Gliding flight in the paradise tree snake, Nature (London) **418**, 603 (2002).

[5] R. L. Hatton and H. Choset, Generating gaits for snake robots: Annealed chain fitting and keyframe wave extraction, Autonomous Robots **28**, 271 (2010).

[6] H. Marvi and D. L. Hu, Friction enhancement in concertina locomotion of snakes, J. R. Soc. Interface **9**, 3067 (2012).

[7] M. H. Dickinson, C. T. Farley, R. J. Full, M. A. R. Koehl, R. Kram, and S. Lehman, How animals move: An integrative view, Science **288**, 100 (2000).

[8] C. Hohenegger and M. J. Shelley, Stability of active suspensions, Phys. Rev. E **81**, 046311 (2010).

[9] S. D. Olson, S. S. Suarez, and L. J. Fauci, Coupling biochemistry and hydrodynamics captures hyperactivated sperm motility in a simple flagellar model, J. Theor. Biol. **283**, 203 (2011).

[10] S. Lim and C. S. Peskin, Fluid-mechanical interaction of flexible bacterial flagella by the immersed boundary method, Phys. Rev. E **85**, 036307 (2012).

[11] S. K. Jones, Y. J. J. Yun, T. L. Hedrick, B. E. Griffith, and L. A. Miller, Bristles reduce the force required to fling wings apart in the smallest insects, J. Exp. Biol. **219**, 3759 (2016).

[12] Y. Bar-Cohen, *Biomimetics: Biologically Inspired Technologies* (CRC Press, Boca Raton, FL, 2005).

[13] B. Jakimovski, *Biologically Inspired Approaches for Locomotion, Anomaly Detection and Reconfiguration for Walking Robots* (Springer, New York, 2011), Vol. 14.

[14] D. T. Roper, S. Sharma, R. Sutton, and P. Culverhouse, A review of developments towards biologically inspired propulsion systems for autonomous underwater vehicles, Proc. Inst. Mech. Eng. M **225**, 77 (2011).

[15] F. Jacob, Evolution and tinkering, Science **196**, 1161 (1977).

[16] R. McNeill Alexander, *Optima for Animals* (Princeton University Press, Princeton, NJ, 1996).

[17] R. B. Langerhans and D. N. Reznick, Ecology and evolution of swimming performance in fishes: Predicting evolution with biomechanics, in *Fish Locomotion: An Eco-Ethological Perspective*, edited by P. Domenici and B. G. Kapoor (CRC Press, Boca Raton, FL, 2010), pp. 200–248.

[18] L. E. Becker, S. A. Koehler, and H. A. Stone, On self-propulsion of micro-machines at low Reynolds number: Purcell's three-link swimmer, J. Fluid Mech. **490**, 15 (2003).

[19] J. E. Avron, O. Gat, and O. Kenneth, Optimal Swimming at Low Reynolds Numbers, Phys. Rev. Lett. **93**, 186001 (2004).

[20] D. Tam and A. E. Hosoi, Optimal Stroke Patterns for Purcell's Three-Link Swimmer, Phys. Rev. Lett. **98**, 068105 (2007).

[21] H. C. Fu, T. R. Powers, and C. W. Wolgemuth, Theory of Swimming Filaments in Viscoelastic Media, Phys. Rev. Lett. **99**, 258101 (2007).

[22] S. E. Spagnolie and E. Lauga, The optimal elastic flagellum, Phys. Fluids **22**, 031901 (2010).

[23] D. Crowdy, S. Lee, O. Samson, E. Lauga, and A. E. Hosoi, A two-dimensional model of low-Reynolds number swimming beneath a free surface, J. Fluid Mech. **681**, 24 (2011).

[24] B. Bittner, R. L. Hatton, and S. Revzen, Geometrically optimal gaits: A data-driven approach, Nonlinear Dyn. **94**, 1933 (2018).
[25] J. Lighthill, *Mathematical Biofluiddynamics* (Society for Industrial and Applied Mathematics, SIAM, Philadelphia, 1975).
[26] S. Childress, *Mechanics of Swimming and Flying* (Cambridge University Press, Cambridge, 1981).
[27] J. A. Sparenberg, *Hydrodynamic Propulsion and Its Optimization: Analytic Theory* (Kluwer Academic Publishers, Dordrecht, The Netherlands, 1994), Vol. 27.
[28] S. Alben, Passive and active bodies in vortex-street wakes, J. Fluid Mech. **642**, 95 (2009).
[29] S. Michelin and S. G. Llewellyn Smith, Resonance and propulsion performance of a heaving flexible wing, Phys. Fluids **21**, 071902 (2009).
[30] J. Peng and S. Alben, Effects of shape and stroke parameters on the propulsion performance of an axisymmetric swimmer, Bioinspiration Biomimetics **7**, 016012 (2012).
[31] M. Gazzola, M. Argentina, and L. Mahadevan, Gait and speed selection in slender inertial swimmers, Proc. Natl. Acad. Sci. USA **112**, 3874 (2015).
[32] Z. V. Guo and L. Mahadevan, Limbless undulatory propulsion on land, Proc. Natl. Acad. Sci. USA **105**, 3179 (2008).
[33] J. Aguilar, T. Zhang, F. Qian, M. Kingsbury, B. McInroe, N. Mazouchova, C. Li, R. Maladen, C. Gong, M. Travers, R. L. Hatton, H. Choset, P. B. Umbanhowar, and D. I. Goldman, A review on locomotion robophysics: The study of movement at the intersection of robotics, soft matter and dynamical systems, Rep. Prog. Phys. **79**, 110001 (2016).
[34] M. Gazzola, L. H. Dudte, A. G. McCormick, and L. Mahadevan, Forward and inverse problems in the mechanics of soft filaments, R. Soc. Open Sci. **5**, 171628 (2018).
[35] H. B. Lillywhite, *How Snakes Work: Structure, Function and Behavior of the World's Snakes* (Oxford University Press, Oxford, 2014).
[36] B. C. Jayne, Mechanical behavior of snake skin, J. Zool. **214**, 125 (1988).
[37] R. A. Seigel, J. T. Collins, and S. S. Novak, *Snakes: Ecology and Evolutionary Biology* (Macmillan, New York, 1987).
[38] D. L. Hu, J. Nirody, T. Scott, and M. J. Shelley, The mechanics of slithering locomotion, Proc. Natl. Acad. Sci. USA **106**, 10081 (2009).
[39] D. L. Hu and M. Shelley, Slithering locomotion, in *Natural Locomotion in Fluids and on Surfaces* (Springer, New York, 2012), pp. 117–135.
[40] D. I. Goldman and D. L. Hu, Wiggling through the world: The mechanics of slithering locomotion depend on the surroundings, Am. Sci. **98**, 314 (2010).
[41] A. A. Transeth, R. I. Leine, C. Glocker, K. Y. Pettersen, and P. Liljebäck, Snake robot obstacle-aided locomotion: Modeling, simulations, and experiments, IEEE Trans. Robot. **24**, 88 (2008).
[42] A. A. Transeth, K. Y. Pettersen, and P. Liljebäck, A survey on snake robot modeling and locomotion, Robotica **27**, 999 (2009).
[43] H. Ohno and S. Hirose, Design of slim slime robot and its gait of locomotion, in *Proceedings of the 2001 IEEE/RSJ International Conference on Intelligent Robots and Systems* (IEEE, New York, 2001), Vol. 2, pp. 707–715.
[44] P. Liljebäck, K. Y. Pettersen, Ø. Stavdahl, and J. T. Gravdahl, A review on modeling, implementation, and control of snake robots, Rob. Auton. Syst. **60**, 29 (2012).
[45] F. L. Chernousko, Modelling of snake-like locomotion, Appl. Math. Comput. **164**, 415 (2005).
[46] G. L. Wagner and E. Lauga, Crawling scallop: Friction-based locomotion with one degree of freedom, J. Theor. Biol. **324**, 42 (2013).
[47] E. Lauga and T. R. Powers, The hydrodynamics of swimming microorganisms, Rep. Prog. Phys. **72**, 096601 (2009).
[48] S. Alben, Optimizing snake locomotion in the plane, Proc. Roy. Soc. London, Ser. A **469**, 20130236 (2013).
[49] G. I. Taylor, Analysis of the swimming of long and narrow animals, Proc. R. Soc. London, Ser. A **214**, 158 (1952).
[50] M. Sfakiotakis and D. P. Tsakiris, Undulatory and pedundulatory robotic locomotion via direct and retrograde body waves, in *IEEE International Conference on Robotics and Automation, ICRA'09* (IEEE, New York, 2009), pp. 3457–3463.
[51] R. D. Maladen, Y. Ding, P. B. Umbanhowar, and D. I. Goldman, Undulatory swimming in sand: Experimental and simulation studies of a robotic sandfish, Int. J. Rob. Res. **30**, 793 (2011).
[52] F. Jing and S. Alben, Optimization of two- and three-link snake-like locomotion, Phys. Rev. E **87**, 022711 (2013).
[53] R. G. Cox, The motion of long slender bodies in a viscous fluid, Part 1. General theory, J. Fluid Mech. **44**, 791 (1970).
[54] X. Wang, M. T. Osborne, and S. Alben, Optimizing snake locomotion on an inclined plane, Phys. Rev. E **89**, 012717 (2014).
[55] X. Wang and S. Alben, Dynamics and locomotion of flexible foils in a frictional environment, Proc. R. Soc. A **474**, 20170503 (2018).
[56] B. Bhushan, *Introduction to Tribology* (John Wiley & Sons, New York, 2013).
[57] V. L. Popov, *Contact Mechanics and Friction* (Springer, New York, 2010).
[58] E. Pennestrì, V. Rossi, P. Salvini, and P. P. Valentini, Review and comparison of dry friction force models, Nonlinear Dyn. **83**, 1785 (2016).
[59] D. D. Quinn, A new regularization of Coulomb friction, J. Vib. Acoust. **126**, 391 (2004).
[60] L. Borello, P. Maggiore, G. Villero, and M. D. L. Dalla Vedova, A comparison between dry friction discontinuous computational algorithms, in the *27th International Congress of the Aeronautical Sciences, ICAS 2010, Nice, France* (Optimage, Ltd., Edinburgh, UK, 2010).
[61] J.-L. Ligier and P. Bonhôte, Few problems with regularized coulomb law, Mech. Ind. **16**, 202 (2015).
[62] F. Gholami, M. Nasri, J. Kövecses, and M. Teichmann, A linear complementarity formulation for contact problems with regularized friction, Mech. Mach. Theory **105**, 568 (2016).
[63] P. Vigué, C. Vergez, S. Karkar, and B. Cochelin, Regularized friction and continuation: Comparison with Coulomb's law, J. Sound Vib. **389**, 350 (2017).
[64] C. T. Kelley, *Iterative methods for Linear and Nonlinear Equations* (Society for Industrial and Applied Mathematics, Philadelphia, 1995).
[65] J. E. Dennis, Jr. and R. B. Schnabel, *Numerical Methods for Unconstrained Optimization and Nonlinear Equations* (Society for Industrial and Applied Mathematics, Philadelphia, 1996), Vol. 16.
[66] J. K. Hopkins, B. W. Spranklin, and S. K. Gupta, A survey of snake-inspired robot designs, Bioinspiration Biomimetics **4**, 021001 (2009).

[67] E. M. Purcell, Life at low Reynolds number, Am. J. Phys. **45**, 3 (1977).

[68] J. E. Avron and O. Raz, A geometric theory of swimming: Purcell's swimmer and its symmetrized cousin, New J. Phys. **10**, 063016 (2008).

[69] J. Dai, H. Faraji, C. Gong, R. L. Hatton, D. I. Goldman, and H. Choset, Geometric swimming on a granular surface, in *Robotics: Science and Systems XII, Ann Arbor, MI*, edited by D. Hsu, N. Amato, S. Berman, and S. Jacobs (Springer Science and Business Media, New York, 2016).

[70] E. Kanso, J. E. Marsden, C. W. Rowley, and J. B. Melli-Huber, Locomotion of articulated bodies in a perfect fluid, J. Nonlinear Sci. **15**, 255 (2005).

[71] R. L. Hatton and H. Choset, Geometric swimming at low and high Reynolds numbers, IEEE Trans. Robot. **29**, 615 (2013).

[72] B. C. Jayne and J. D. Davis, Kinematics and performance capacity for the concertina locomotion of a snake (coluber constrictor), J. Exp. Biol. **156**, 539 (1991).

[73] J. B. Keller and M. S. Falkovitz, Crawling of worms, J. Theor. Biol. **104**, 417 (1983).